Geochemistry Geophysics Geosystems G3
AN ELECTRONIC JOURNAL OF THE EARTH SCIENCES
Published by AGU and the Geochemical Society

Article
Volume 6, Number 8
25 August 2005
Q08009, doi:10.1029/2005GC000945
ISSN: 1525-2027

Secondary Hawaiian volcanism formed by flexural arch decompression

Todd Anthony Bianco, Garrett Ito, Janet M. Becker, and Michael O. Garcia,
Department of Geology and Geophysics, School of Ocean and Earth Science and Technology, University of Hawaii, Manoa, Post 735, 1680 East-West Road, Honolulu, Hawaii 96822, USA (tbianco@hawaii.edu)

[1] This paper explains two forms of secondary Hawaiian volcanism (rejuvenated onshore and Hawaiian Arch offshore) as a direct consequence of lithospheric flexural uplift that surrounds growing shield volcanoes. This uplift decompresses the underlying asthenosphere, which is assumed to be chemically and isotopically heterogeneous, near its solidus, and derived from the Hawaiian mantle plume. Lithospheric uplift is modeled as the axisymmetric response of an elastic plate to a (volcanic) point load that grows linearly in time. To model flow in the asthenosphere, the rate of flexure of the lithosphere is taken as the upper boundary condition on an isoviscous, incompressible, fluid half-space. This model successfully explains the majority of spatial gaps between secondary and active shield volcanism due to the flexing of a lithospheric plate with an effective elastic thickness of 25–35 km. Second, this work demonstrates that the flexural model can produce realistic magmatic fluxes if magma is focused toward individual eruption sites from the mantle over an area two to ten times the eruption area. Next, this model addresses the isotopic distinction between secondary and shield lavas. In this model, the same heterogeneous mantle plume feeds the secondary and shield lavas, but the compositional components are sampled by melting at rates that differ between the two settings. Flexural decompression mostly melts the component that begins melting shallowest, which we assume to be depleted in incompatible elements with relatively low $^{87}Sr/^{86}Sr$ and high $^{143}Nd/^{144}Nd$. Melting in the center of a mantle plume is assumed to generate shield volcanism and is predicted to mostly melt components that begin melting deepest, which we assume to be enriched in incompatible elements with higher $^{87}Sr/^{86}Sr$ and lower $^{143}Nd/^{144}Nd$. Thus the models successfully predict the observed mean $^{87}Sr/^{86}Sr$ and $^{143}Nd/^{144}Nd$ isotopic compositions of secondary and shield lavas to arise out of the melting process alone. The fourth feature addressed is that secondary lavas are alkalic, having formed from relatively low extents of partial melting, and shield lavas are dominantly tholeiitic, consistent with more extensive partial melting. Indeed, models predict lower mean extent of melting for secondary lavas compared to shield lavas if the source material, which is mostly peridotite, contains at least some pyroxenite. Results show that model predictions are consistent with the geochemical constraints for a range of reasonable starting mantle compositions, lithospheric thicknesses, and plume temperatures.

Components: 13,305 words, 12 figures, 3 tables.

Keywords: Hawaiian Arch; lithospheric flexure; rejuvenation; secondary volcanism.

Index Terms: 1009 Geochemistry: Geochemical modeling (3610, 8410); 3037 Marine Geology and Geophysics: Oceanic hotspots and intraplate volcanism.

Received 8 February 2005; **Revised** 14 May 2005; **Accepted** 3 June 2005; **Published** 25 August 2005.

Bianco, T. A., G. Ito, J. M. Becker, and M. O. Garcia (2005), Secondary Hawaiian volcanism formed by flexural arch decompression, *Geochem. Geophys. Geosyst.*, *6*, Q08009, doi:10.1029/2005GC000945.

1. Introduction

[2] The Hawaiian Islands, near the center of the Pacific plate (Figure 1), are commonly believed to be formed by a mantle plume [*Wilson*, 1963]. Four stages of volcanism have been described for Hawaiian volcanoes [*Moore et al.*, 1982; *Macdonald et al.*, 1983; *Clague and Dalrymple*, 1987]. Growth begins with the alkalic preshield stage and continues with the tholeiitic main shield stage, followed by alkalic postshield volcanism. These stages are likely caused by melting of the plume, with the main shield stage occurring at the center of the plume. The final, or the rejuvenated stage of volcanism, has produced alkalic eruptions on at least six Hawaiian Islands (Niihau, Kauai, Oahu, Molokai, Kahoolawe, and Maui). The cause of this final stage is not well understood.

[3] A defining characteristic of rejuvenation volcanism is that it follows a period (>0.25 to 2.5 Myr) of volcanic quiescence. This temporal hiatus between shield and rejuvenation volcanism also results in a spatial gap since the Pacific plate is moving (~10 cm/yr) relative to the hot spot center, where the shields are built [*Clague and Dalrymple*, 1987; *Garcia et al.*, 1987]. Figure 2 shows the current distance of volcanoes from the presumed location of the hot spot, beneath Kilauea [*Clague and Dalrymple*, 1987, 1988; *Tagami et al.*, 2003; *Ozawa et al.*, 2005]. Note that rejuvenation on one island occurs during the shield stage of a volcano on another island. This plot also includes a fifth type of Hawaiian eruption, the North and South Arch Volcanic Fields [*Lipman et al.*, 1989; *Clague et al.*, 1990; *Dixon et al.*, 1997]. The spacing and timing of the North and South Arch volcanic fields with respect to the concurrently active shield volcanoes suggests that they are offshore versions of rejuvenated volcanism.

[4] A second characteristic of rejuvenation lavas is that the eruptive volume flux is orders of magnitude smaller than at the shield [*Walker*, 1990]. The North Arch lavas cover an expansive area ($\sim 2.5 \times 10^4$ km^2), but are estimated to be only tens of meters thick on average [*Clague et al.*, 2002]. This indicates that both onshore and offshore eruptions are relatively small compared to the shield stage of volcanism which accounts for ~95–98% of a Hawaiian volcano's mass [*Macdonald et al.*, 1983; *Clague and Dalrymple*, 1987].

[5] Another characteristic of rejuvenation lavas is that they are isotopically distinct from the shield stage; for example they have higher $^{143}Nd/^{144}Nd$ and lower $^{87}Sr/^{86}Sr$ values than shield lavas [*Roden et al.*, 1984; *Clague and Dalrymple*, 1988; *Lassiter et al.*, 2000; *Yang et al.*, 2003] (Figure 3). Arch lavas are isotopically similar to the onshore rejuvenation lavas [*Clague et al.*, 1990; *Dixon et al.*, 1997; *Frey et al.*, 2000; *Yang et al.*, 2003]. Hence both arch and rejuvenation lavas are isotopically distinct from shield lavas.

[6] Finally, a fourth characteristic of both the arch and rejuvenated lavas is that their major-element compositions are moderately to strongly alkalic [*Lipman et al.*, 1989; *Clague et al.*, 1990]. This characteristic is distinct from the voluminous tholeiitic shield stage of volcanism in which case the dominant rock type (>90%) is tholeiitic [*Macdonald et al.*, 1983]. Many factors affect the major element composition of magma, such as source composition, melting pressure [*McBirney*, 1993], and the concentration of volatiles [e.g., *Asimow et al.*, 2004]. These factors in concert with the degree of partial melting [*Mysen and Kushiro*, 1977] control the tholeiite-alkalic lava distinction. As would be the case with all other factors equal, the tholeiitic-to-alkalic change has been interpreted to reflect high degrees of partial melting at the hot spot center and lower degrees of partial melting during rejuvenated volcanism [*Clague and Frey*, 1982; *Chen and Frey*, 1983; *Frey et al.*, 1991].

[7] Above, we have listed four similarities between rejuvenated and arch volcanism that distinguish them from shield volcanism. We will thus consider rejuvenation and arch volcanism as the same type of volcanism, and refer to them collectively as "secondary" volcanism [*Stearns*, 1967]. Correspondingly, we propose that models to explain secondary volcanism are better if they predict both onshore and offshore forms, as well as their geochemical differences from shield volcanism.

[8] Three geophysical models have been proposed for onshore secondary volcanism. The most recent model, a dynamic plume model [*Ribe and Christensen*, 1999], has a small second melting zone downstream from the hot spot. This second zone of melting results from upwelling and decompression of the mantle plume layer as it interacts with the overlying lithosphere. This model successfully predicts a spatial gap between hot spot and rejuvenation eruptions. The model also predicts low extents of melting for rejuvenation lavas and higher extents of melting at the hot spot center. The weaknesses of this model are that it does not predict arch volcanism well away from the axis of

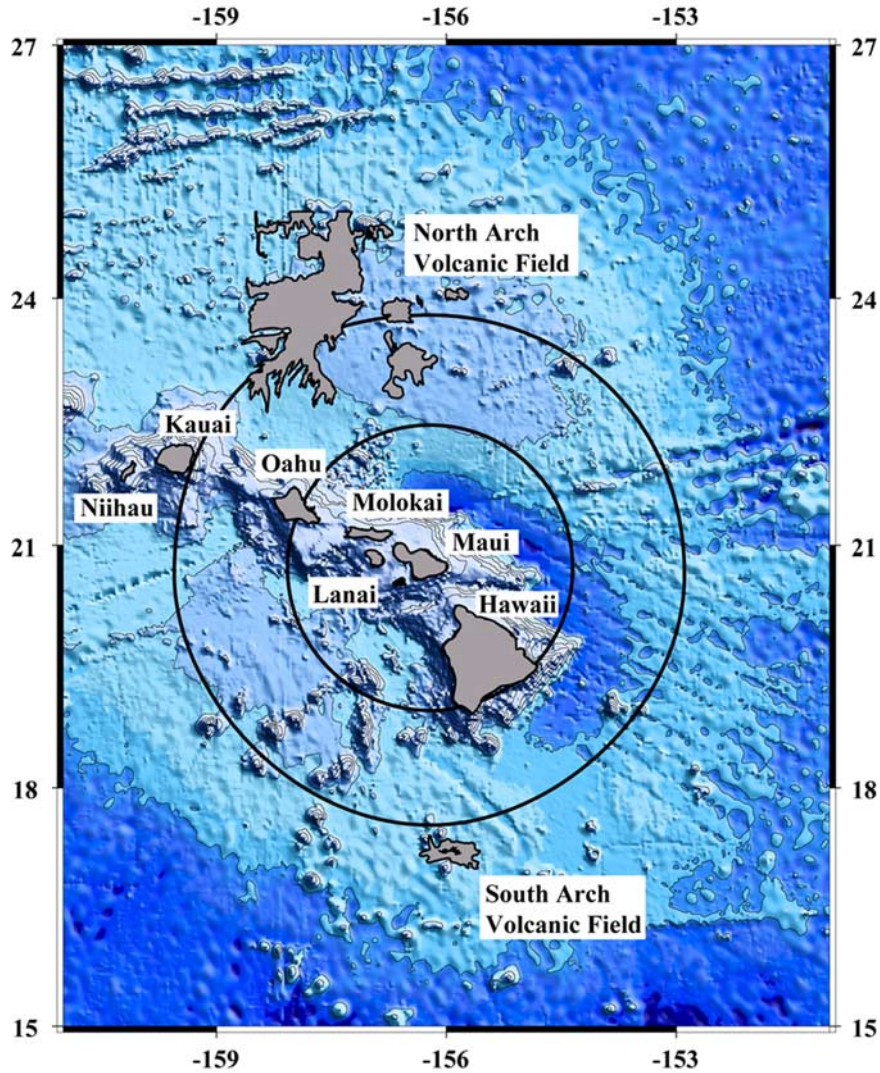

Figure 1. Map of the Hawaiian Islands and the surrounding Pacific plate. The Hawaiian Arch volcanic fields, which straddle the raised bathymetry of the Hawaiian Arch, are also shown. The inner black circle indicates the radius at which plate flexure due to a point load at the summit of Haleakala Volcano changes from downward deflection to upward deflection (assuming elastic plate thickness T_e = 30 km). The outer black circle encloses radii where positive deflection >10% of the maximum flexure.

the island chain nor does it address the isotope compositions of the secondary volcanism.

[9] In a second model [*Gurriet*, 1987; *Liu and Chase*, 1991], the lithosphere is rapidly thinned at the hot spot [*Detrick and Crough*, 1978; *Crough*, 1978] and then melts as it is conductively heated by the anomalously hot, underlying asthenosphere. This model predicts relatively small volumes of rejuvenation lavas compared to shield volcanism, invokes melting of the lithosphere to explain the isotopic character of rejuvenation lavas, and predicts low extents of melting as prescribed for alkalic lavas. The weaknesses of this model are that it does not predict the temporal gap typically preceding rejuvenation volcanism or the presence of volcanism on the South Arch.

[10] The third model attributes rejuvenated volcanism to lithospheric flexure [*Jackson and Wright*, 1970; *Moore*, 1970; *Clague and Dalrymple*, 1987; *ten Brink and Brocher*, 1987]. The growing load of an active shield pushes and flexes the underlying lithosphere downward with upward flexing occurring some radial distance away from the load (Figure 1). This process generates the Hawaiian moat and flexural arch surrounding the island chain, as are evident in bathymetric and gravity studies near Hawaii [e.g., *Watts et al.*, 1985; *Wessel*, 1993] and at other hot spots [*McNutt and*

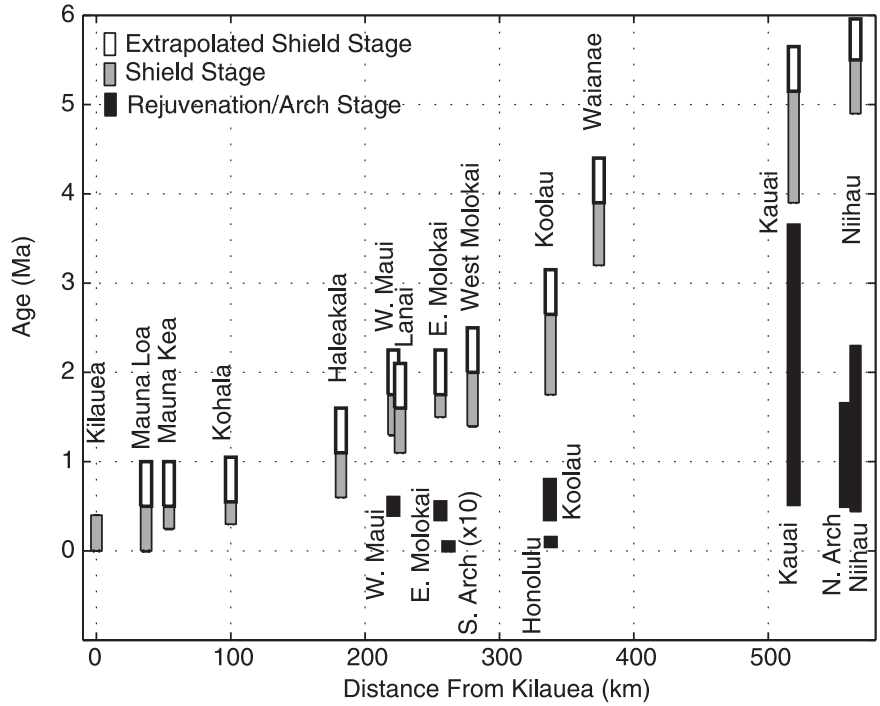

Figure 2. Age span of Hawaiian volcanism, subdivided into stages and plotted versus distance from Kilauea Volcano (modified from *Clague and Dalrymple* [1987], including data from *Clague and Dalrymple* [1988], *Lipman et al.* [1989], *Clague et al.* [2002], *Tagami et al.* [2003], and *Ozawa et al.* [2005]). Black bars represent secondary volcanism, gray bars represent shield volcanism, and white bars represent extrapolated shield stage (uniformly 500 ka to conservatively estimate the duration of shield volcanism [e.g., *Lipman*, 1995; *Guillou et al.*, 1997]). No extrapolation is added to the young Kilauea Volcano [e.g., *DePaolo and Stolper*, 1996; *Quane et al.*, 2000]. The time span of South Arch volcanism is vertically exaggerated by a factor of ten for visibility. This time span represents the black region of the South Arch field in Figure 1, where the outer gray region maps flows that are probably older than the inner flows but young relative to other Hawaiian volcanism [see *Lipman et al.*, 1989].

Menard, 1978]. *Clague and Dalrymple* [1987] noted that the distance (or temporal) gap between shield volcanism and rejuvenation volcanism is similar to the distance (or temporal) gap between loading islands and the flexural arch. *Ten Brink and Brocher* [1987] proposed that stresses in the flexed lithosphere near the arch would allow pooled melt at the base of the crust to penetrate the lithosphere and erupt. The physical mechanism that produces melt beneath the flexural arches and the geochemical consequences, however, have not been explored quantitatively.

[11] A successful model of secondary volcanism should predict the four key observations outlined above: (1) a spatial gap between the shield stage and secondary volcanism, (2) small volumes of secondary volcanism compared to the shield stage, and broad eruption areas in the case of arch lavas, (3) the observed isotopic distinction between secondary lavas and shield lavas, (4) a major-element distinction between alkalic secondary and the tholeiitic shield lavas. This paper develops a quantitative model in which the growth of an active shield causes the rise of a flexural arch surrounding the active load. We develop analytical solutions of lithospheric flexure and asthenospheric decompression, and combine them with a geochemical model that describes the melting of a heterogeneous mantle plume. Our model addresses each of the above characteristics of rejuvenated volcanism.

2. Spatial and Temporal Correlations With Active Shields

[12] In this section, we test whether flexure can explain the separation in distance between an active shield and secondary volcanism. Figure 2 shows the time and distance of shield and secondary events relative to the active hot spot center. We measure the distances from the approximate center of rejuvenation to the approximate center of mass of any shield that was contemporaneously loading. It is clear that the age span of a given volcanic event often overlaps with the shield stage of

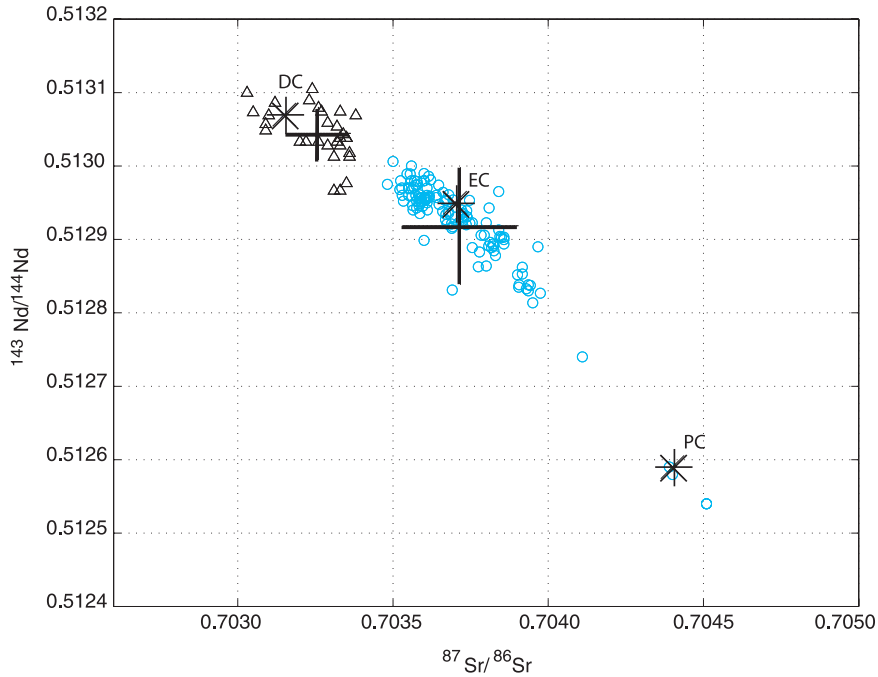

Figure 3. $^{143}Nd/^{144}Nd$ and $^{87}Sr/^{86}Sr$ isotope data for Hawaiian secondary (black triangles) [*Okano and Tatsumoto*, 1996; *Reiners and Nelson*, 1998; *Lassiter et al.*, 2000; *Frey et al.*, 2000] and shield lavas (blue circles; http://georoc.mpch-mainz.gwdg.de). Average values and one standard deviation in both Nd and Sr isotope systems are marked with a black cross. Arbitrarily assumed mean compositions of DC (I_o^{DC}) and EC (I_o^{EC}) and PC I_o^{PC} used in the reference model are shown by large asterisks.

multiple volcanoes. For example, the shield stage of Mauna Loa, Mauna Kea, and Kohala all occurred during the time span of rejuvenation on East Molokai (Figure 2). As all of these shields could contribute to flexural uplift on East Molokai (although not necessarily precisely at the same time), we plot the distance between East Molokai and each of the three shields (Figure 4a). The same measurements are repeated for all of the other rejuvenation events. To be conservative, we lengthen the time span of shield building beyond that inferred from dated subaerial lava samples to reflect indications that the duration of the shield stage may be as long as 1.4 Myr (shown as white rectangles) [e.g., *Lipman*, 1995; *Guillou et al.*, 1997]. However, we do not extend the time span of the shield stage of Kilauea Volcano because it is still relatively young [e.g., *DePaolo and Stolper*, 1996; *Quane et al.*, 2000]. The data indicate what others also have recognized: rejuvenation may occur contemporaneously over a large distance, but the data also indicates onshore secondary volcanism occurs most frequently at radial distances of about 200–400 km from shield stage volcanism. Offshore secondary volcanism often occurs at slightly greater distances but most frequently within ~250–500 km.

[13] To test whether these distances occur on the flexural arch, we now solve for the rate of lithospheric flexure of an elastic plate due to a linearly (in time) growing, transverse load [*Nadai*, 1931]. Combining the constitutive law for bending of a thin elastic plate with the momentum equation, we obtain

$$\nabla^4 w + \frac{\Delta\rho g}{D} w = 0 \tag{1}$$

at all, nonzero, radial distances, r, from the point load. In (1), $w(r, t)$ is downward displacement, $\Delta\rho$ is the density contrast between the mantle and water, g is gravitational acceleration, D is flexural rigidity, and ∇^4 is the biharmonic operator (see also Table 1 for definition of variables). Taking the time derivative of (1), *Nadai*'s [1931] solution provides the rate of flexure due to a growing point load. The solution is

$$\dot{w} = \frac{\dot{Q}}{4\sqrt{\Delta\rho g D}} [\mathrm{Re} J_o(r') - \mathrm{Im} Y_o(r')], \tag{2}$$

where $\dot{w}$ is the vertical displacement rate and, $\dot{Q}$ is the rate of growing force exerted by the concentrated point load on the plate, ReJ_0 is the real part

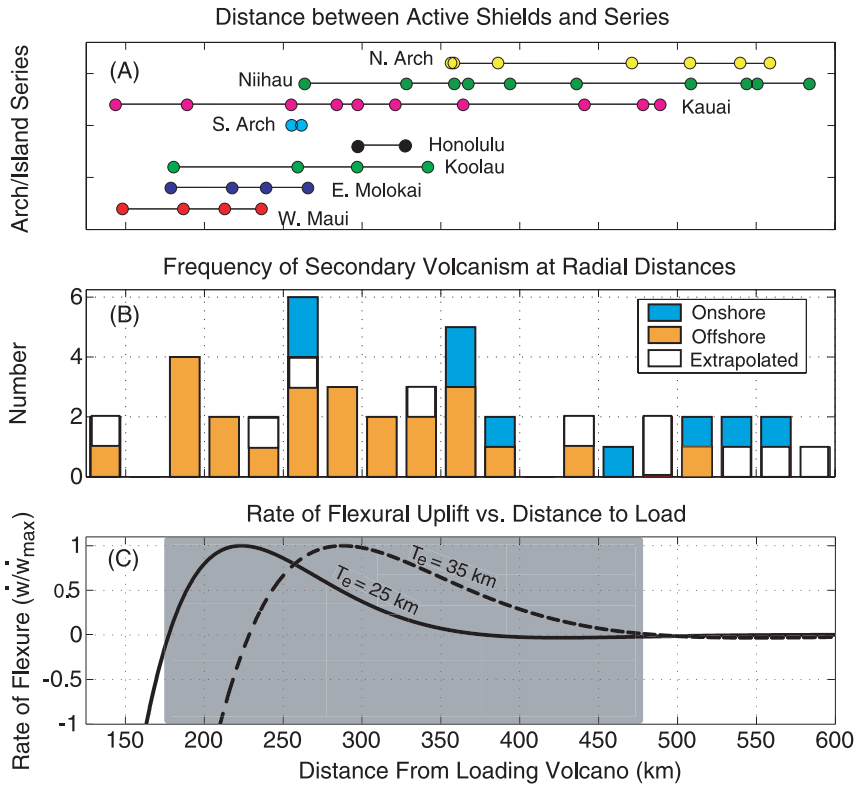

Figure 4. The shield and secondary volcanism spatial relationship. (a) Circles show the distance between the labeled rejuvenation or arch series and the multiple, contemporaneously active shield volcanoes. (b) A histogram of the population of shields active during secondary volcanism grouped by radial distance between the two types of volcanism. White bars are population data derived from the extrapolation of shield ages as in Figure 2. (c) Normalized lithospheric rate of flexure profiles predicted (with equation (2)) for effective elastic plate thickness of 25 km (solid) and 35 km (dashed). Gray shading shows the potential radial span of flexural uplift.

of a (zeroth-order) Bessel function of the first kind, and ImY_0 is the imaginary part of a (zeroth-order) Bessel function of the second kind. ReJ_0 and ImY_0 are functions of radial distance r normalized by the flexural parameter α,

$$r' = \frac{r\sqrt{i}}{\alpha}, \tag{3}$$

where $i = \sqrt{-1}$. The flexural parameter α depends on flexural rigidity D according to [*Nadai*, 1931]

$$\alpha = \left(\frac{D}{\Delta\rho g}\right)^{1/4} \tag{4}$$

and D depends on effective elastic plate thickness T_e according to

$$D = \frac{ET_e^3}{12(1-\eta^2)}, \tag{5}$$

where E is Young's modulus and η is Poisson's ratio.

[14] From (3)–(5) it is clear that the distance to and width of the arch depends on D and T_e. The effective elastic plate thickness is a quantity that describes the flexural strength of the plate; it depends on the depth-integrated strength of a visco-elastic lithosphere [*McNutt*, 1984] but need not correspond to a real depth in the lithosphere. Figure 4c shows predicted flexure profiles for T_e = 25 and 35 km. This range of T_e is consistent with other estimates of the elastic plate thickness near Hawaii [*Watts et al.*, 1985; *Wessel*, 1993] and predicts flexural uplift at distances from the loading shield that overlap substantially with the distance of most frequent secondary volcanism. While some secondary volcanism may have occurred outside of the predicted region, the majority of the secondary events are consistent with the flexure model for T_e = 25 to 35 km.

3. Melting Model

3.1. Conceptual Model Description

[15] In this section, we explore the fluxes and compositions of volcanism that flexural arch de-

Table 1. General Constants and Variables

Symbol	Meaning	Assumed Values	Units
$\mathcal{B}$	vector potential		
C_o^i	initial concentration in component i relative to primitive mantle		
D	flexural rigidity	9.72×10^{22}–26.7×10^{22}	N · m
E	Young's modulus	70[a]	GPa
E^i	enrichment of lithology i		
F	extent of partial melting		
$\mathcal{F}$	Fourier transform operator		
F_v	mean degree of partial melting		
g	gravitational acceleration	9.8	m/s^2
$\dot{h}_{cr}^i$	rate of crustal thickening at flexural arch		m/s
$\overline{H}_{cr}$	average rate of crustal thickening per increment of arch uplift		s^{-1}
I_o^i	initial isotopic ratio of component i		
I^f	final isotopic ratio		
i	$\sqrt{-1}$		
J_0	Bessel function of the first kind, order zero		
k	normalized wave number vector magnitude		
k_D	bulk distribution coefficient		
$\dot{M}_{arch}$	melt production rate beneath flexural arch		m/s
$\dot{M}_{shield}$	melt production rate beneath the shield		m^2/s
n	number of components in mantle	3	
p	pressure		Pa
$\overline{p}$	dynamic pressure		Pa
$\dot{Q}$	rate of growing point load		N/s
$\mathbf{r}$, r, r_+	radial vector, radial distance, and radial distance range for positive flexural uplift		m
r'	normalized radial distance		
t	time		s
T_e	effective elastic plate thickness	25–35[b,c]	km
$\overline{T}_P$	mean starting potential temperature of the unmelted mantle plume	1400–1700	°C
T_a	adiabatic temperature		°C
$\mathbf{v}$, v_r, v_z	velocity vector, radial component, and upward component		m/s
v_r	first-order Hankel transform of radial velocity beneath the flexural arch		m^3/s
v_z	zeroth-order Hankel transform of vertical velocity beneath flexural arch		m^3/s
$\mathcal{V}_z$	Fourier transform of vertical velocity beneath flexural arch		m^2/s
w	lithospheric deflection		m
$\dot{w}$	lithospheric deflection rate		m/s
$\dot{w}$	zeroth-order Hankel transform of lithospheric deflection rate		m^3/s
X	mass fraction of original solid source extracted by melting		
Y_0	Bessel function of the second kind, order zero		
$\mathbf{z}$, z	depth vector and depth below seafloor at $r \rightarrow \infty$		m
z'	depth below base of lithosphere at $r \rightarrow \infty$		m
z_1, z_2	depth of base of plume, base of lithosphere		m
α	flexural parameter	44.6–58.7	km
ϕ^i	starting mass fraction of component i in unmelted source		
Φ	critical mass porosity in the mantle	0.01[d,e]	
η	Poisson's ratio	0.25	
μ	dynamic viscosity	10^{20}	Pa · s
ρ	density of asthenosphere	3300[a]	kg/m^3
ρ_L	density of crust and magma	2800[a]	kg/m^3
ρ_w	density of water	1000	kg/m^3
$\Delta\rho$	$\rho - \rho_w$	2300	kg/m^3
ξ	normalized Hankel transform parameter		m^{-1}
ξ_{max}	summation limit of ξ (equation (14))	0.0048	m^{-1}
$\Delta\xi$	summation interval of ξ (equation (14))	2e-7	m^{-1}
ψ	stream function		
Ψ, $\hat{\Psi}$	azimuthal component of vector potential and corresponding first-order Hankel transform		

[a] *Turcotte and Schubert* [2002].
[b] *Watts et al.* [1985].
[c] *Wessel* [1993].
[d] *Sims et al.* [1999].
[e] *Pietruszka et al.* [2001].

compression can generate. Before describing the mathematical model in detail, we first provide a conceptual overview. This model assumes the plume material is hot and chemically heterogeneous [e.g., *Frey and Rhodes*, 1993; *Hauri et al.*, 1996; *Lassiter and Hauri*, 1998; *Frey et al.*, 2005]. The hot material in the mantle plume stem upwells and melts at the hot spot center to create shield volcanism (Figure 5). It is assumed that the melting stops as the buoyant material is diverted sideways at the base of the rigid lithosphere, thus the plume melting region ends where all buoyant upwelling is zero. Material then flows horizontally (downstream from the hot spot and away from the axis of the island chain) beneath the lithosphere and forms a layer beneath the arch. If the lateral flow is rapid, this material has lost little heat due to conduction. Consequently, the solid residue remains everywhere at its solidus, while the liquid residue is at the critical porosity [*Langmuir et al.*, 1977; *McKenzie*, 1985] that could not be extracted beneath the shield. Thus any further decompression can cause further melting, melt extraction, and secondary magmatism.

[16] The building of a new shield volcano at the hot spot center triggers this additional decompression under the flexural arch both along the island chain (onshore rejuvenated volcanism) and well away from the chain (e.g., the North and South Arch) by drawing asthenosphere upward beneath the arch (Figure 1). A simple way to visualize this is to consider an unflexed lithosphere as the initial state. The pressure in the asthenosphere is hydrostatic (fluid is motionless) and by definition, all points at a given depth (e.g., $z' = z'_o$) have the same pressure (otherwise, the fluid would move). When the surface is flexed upward at the arch, it causes the asthenosphere to rise (Figure 5). After the flexing at the arch stops, the pressure in the asthenosphere is again hydrostatic regardless of the shape of the surface. As before, pressure is equal at all points at a given depth below a reference depth. This reference depth does not depend on r, but rather is the depth beneath the unflexed lithosphere at $r \rightarrow \infty$ (i.e., where material has not moved). In light of this description, it is important to formally define a depth variable z' as the depth beneath the unflexed lithosphere at $r \rightarrow \infty$. Thus material under the arch that started at z'_o is now at shallower depth of z'_f, and has experienced a negative pressure change of $\sim\rho(z'_f - z'_o)$ (see discussion of equation (7) below). We will show the upwelling beneath the rising arch varies predictably as a function of depth below the lithosphere z', and determines the flux of magma generated. Furthermore, the pattern of mantle upwelling beneath the flexing arch is distinct from that beneath the hot spot center. This difference influences the rate and extent of partial melting of the different mantle source components and thus the isotopic and major-element distinctions between secondary and shield volcanism. Therefore the distinct isotopic compositions between the two volcanic stages arise by different mantle flow and melting conditions, which extract different proportions of source components from the same initial heterogeneous mantle.

3.2. Mantle Flow Driven by Plate Flexure

[17] We model the asthenosphere as an incompressible, isoviscous fluid. The asthenosphere fills an axisymmetric half-space, bounded above by the flexing lithosphere. In a viscous (asthenospheric) fluid of zero Reynolds number (zero acceleration), the invariant form of the Navier-Stokes equation describes the momentum balance

$$\nabla \overline{p}(r, z') = \mu \nabla^2 \mathbf{v}(r, z'), \tag{6}$$

where r is radial distance from the growing shield volcano and z' is depth below the base of the unflexed lithosphere at $r \rightarrow \infty$ (Figure 5). The variable $\overline{p}(r, z') = p(r, z') - \rho g z'$ is the dynamic pressure, p is total pressure (in excess of that beneath the unflexed lithosphere), ρ is the density of the asthenosphere, μ is the dynamic viscosity (constant), and $\mathbf{v}(r, z') = (v_r(r, z'), 0, v_z(r, z'))$ is the velocity vector in cylindrical coordinates (r, θ, z'). Melting of the asthenosphere is controlled by the rate of decompression

$$\frac{Dp}{Dt} = \frac{D\overline{p}}{Dt} + \rho g v_z = \mathbf{v} \cdot \mu \nabla^2 \mathbf{v} + \rho g v_z \tag{7}$$

Because we have chosen to model time-independent loading, the rate of the dynamic pressure release is only the advective term, $\mathbf{v} \cdot \mu \nabla^2 \mathbf{v}$, of the material time derivative $\frac{D\overline{p}}{Dt}$. To compare the rate of dynamic pressure loss to the decrease in lithostatic pressure, we define the velocity scale to be the maximum rate of flexure (solved in the following steps), the length scale to be the flexural parameter α, and assume $\mu = 10^{19}$ Pa·s. The result is the second term is $\geq 10^6$ times larger than the first term, so Dp/Dt is well approximated be $\rho g v_z$. Dp/Dt is negative for negative v_z, or upwelling, therefore we must solve for the velocity field driven by lithospheric flexure.

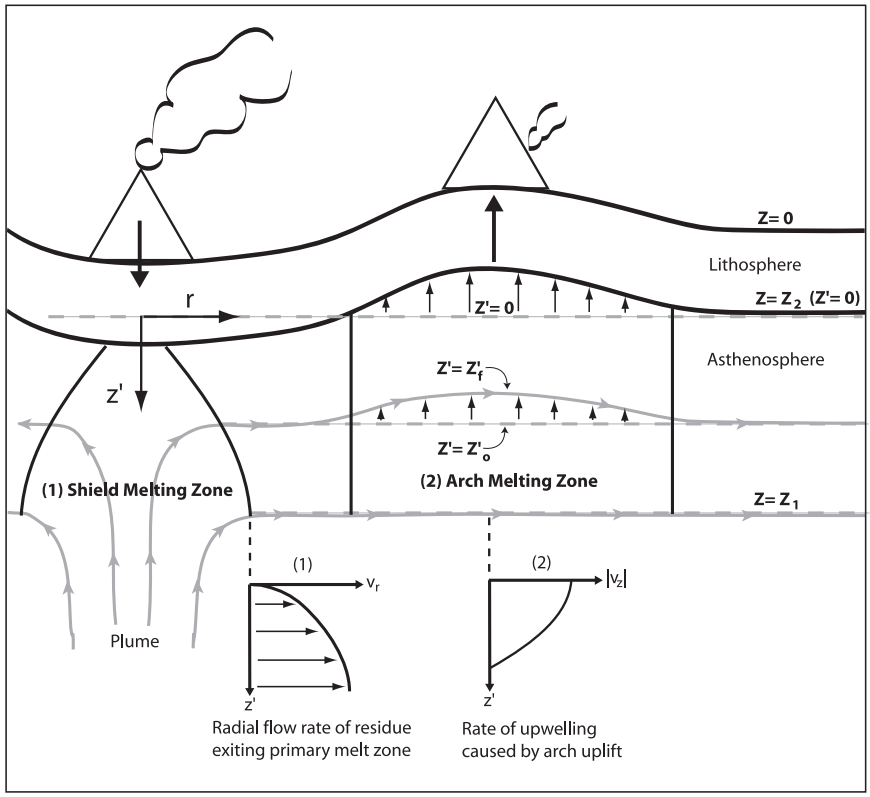

Figure 5. A schematic of the flexure model for Hawaiian secondary volcanism. Growth of the active shield pushes downward (large downward pointing arrow) on the lithosphere beneath the shield and causes flexural uplift (large upward pointing arrow) and secondary volcanism away from the shield. The black curved lines are an exaggerated example of how the lithosphere will flex compared to the unloaded lithosphere (top dashed line). The gray solid lines are streamlines in the asthenosphere. Dashed gray lines are examples of reference depths and approximately define isobars such that as material is displaced above them, it melts at a rate that is proportional to the upwelling rate (see equation (7)). The most shallow, dashed, gray line is the depth of the base of the unflexed lithosphere at $r \rightarrow \infty$ and is the reference depth defining $z' = 0$. Arch uplift draws material from an initial depth of $z' = z'_o$ to a shallower level of $z' = z'_f$ and therefore decompresses this material by $\sim\rho(z'_f - z'_o)$. Inset (2) shows the upwelling rate $v_z(z')$ as a function of z' at each point of the flexural arch (see equation (14) and Figure 8a). Because $|v_z(z')|$ is larger near the base of the lithosphere arch, melting will heavily sample material melting in the upper portion of the melting zone (i.e., DC melts). Inset (1) shows the rate at which residue is exiting the shield melting zone [see *Ito and Mahoney*, 2005] and therefore indicates the rate of melt extracted as averaged over the entire shield melting zone (Figure 8a). In contrast to arch melting, shield melting above the plume stem will more heavily extract melts near the base of the melting zone (i.e., EC and PC).

[18] The continuity equation for an incompressible fluid takes the invariant form

$$\nabla \cdot \mathbf{v} = 0. \tag{8}$$

For axisymmetric motion of the incompressible asthenosphere, we introduce a stream function, ψ, according to

$$\mathbf{v}(\mathbf{r}, \mathbf{z}) = \nabla \times \mathbf{B}, \tag{9}$$

where $\mathbf{B} = (0, \psi/r, 0)$. The vorticity equation for the stream function is obtained by taking the curl of (6) which yields a biharmonic equation:

$$\nabla^4 \mathbf{B} = 0. \tag{10}$$

[19] To determine the asthenospheric flow generated by the flexural uplift, we solve (10) subject to the boundary conditions at the surface of the asthenosphere ($z' = 0$)

$$v_z = \frac{1}{r}\frac{\partial \psi}{\partial r} = \dot{w}, \quad z' = 0 \tag{11}$$

$$v_r = -\frac{1}{r}\frac{\partial \psi}{\partial z} = 0, \quad z' = 0 \tag{12}$$

and at $z' \rightarrow \infty$,

$$v_r \rightarrow 0, \quad v_z \rightarrow 0, \quad z' \rightarrow \infty. \tag{13}$$

Equations (11) and (12) describe the continuity of vertical velocity and the no slip condition at the lithospheric-asthenospheric boundary. We do not include the effects of the motion of the Pacific Plate relative to the hot spot reference frame because this contributes only horizontal asthenospheric flow, which for the uniformly viscous fluid modeled here, has no influence on the vertical and melting.

[20] Equations (10) through (13) may be solved analytically using Hankel transforms as in Appendix A [see also *Sneddon*, 1951, pp. 307–310]. Appendix B describes the formulation and solution of (1) using Hankel transforms, so that the rate of lithospheric flexure may be applied as a boundary condition on the asthenospheric half-space (equation (11)). The solution given by (A8) is evaluated by numerical integration using the trapezoid rule expressed as the following discrete summation

$$v_z(r,z') = \frac{\dot{Q}}{2\pi\Delta\rho g}\left\{\sum_{\xi=0}^{\xi_{max}-\Delta\xi}\left[\frac{\xi^2 z' + \xi}{(\alpha\xi)^4 + 1}\right]e^{-\xi z'}J_0(\xi r) + \sum_{\xi=\Delta\xi}^{\xi_{max}}\left[\frac{\xi^2 z' + \xi}{(\alpha\xi)^4 + 1}\right]e^{-\xi z'}J_0(\xi r)\right\}\frac{\Delta\xi}{2}. \quad (14)$$

Here ξ is the transform parameter describing the "wavelength" of radial variations in v_z (analogous to wave number in a Fourier transform), $\Delta\xi$ is the interval of ξ used in the numerical integration, and ξ_{max} is the upper limit of the summation (values necessary for acceptable convergence are listed in Table 1).

[21] We confirm this solution using an independent method involving Fourier transforms. We take the 2-D Fourier transform of (2) in Cartesian coordinates. Incompressible flow forced by this surface boundary condition [*Turcotte and Schubert*, 2002, p. 239, equation (6–92)] in Fourier space is

$$\mathcal{V}_z(k,z') = \mathcal{F}\left\{\frac{\dot{Q}}{4\sqrt{\Delta\rho g D}}[\mathrm{Re}J_o(r') - \mathrm{Im}Y_o(r')]\right\}e^{-kz'}(1+k). \quad (15)$$

Here $\mathcal{V}_z$ is the 2-D (x-y) Fourier transform of v_z, k is the magnitude of the horizontal wave number vector, and $\mathcal{F}$ is the Fourier transform operator. An inverse Fourier transform of (15) produces an independent check on v_z from (14), showing agreement within a maximum error of $<10^{-4}$ of the peak vertical velocity at $z' = 0$.

[22] An example solution for v_z is shown in Figure 6 (where upwelling is >0.1 of the maximum upward velocity of the asthenosphere beneath the rising arch, $\dot{w}_{max}$). The flexing lithosphere drives the flow of the asthenosphere and therefore the most rapid flow is at the surface of the asthenosphere. Upwelling decays (equations (14) and (15)) with depth z', but still remains ~40% of the lithosphere velocity at 70 km below the lithosphere, which we subsequently demonstrate encompasses most of the reference model melting zone.

3.3. Melting Beneath the Flexural Arch

[23] The volume and composition of melts is computed by combining the above solutions for asthenospheric decompression with the melting model. The model, based on that of *Ito and Mahoney* [2005], considers a heterogeneous mantle with up to three source components. Studies show that two or more sources are present in a heterogeneous Hawaiian plume [e.g., *Staudigel et al.*, 1984; *Chen and Frey*, 1985; *Frey et al.*, 2005]. Indeed we have found that three (rather than two) components best satisfy the geochemical as well as physical criteria that define acceptable solutions presented below, however our purpose is not to argue for the number of components, but rather to illustrate how the more successful case behaves. The first, a depleted component (DC) [*Frey et al.*, 2005], is assumed to be anhydrous peridotite that has a lower concentration of Sr and Nd relative to primitive mantle [e.g., *Sun and McDonough*, 1989], has a relatively low $^{87}Sr/^{86}Sr$ and a high $^{143}Nd/^{144}Nd$ isotope ratio (see Table 2 for values assumed), and begins melting shallowest with the solidus defined empirically by *Hirschmann* [2000]. The second component is pyroxenite (PC); it is assumed to have a higher concentration of Sr and Nd relative to primitive mantle, and it has a relatively high $^{87}Sr/^{86}Sr$ and low $^{143}Nd/^{144}Nd$ isotope ratio. Pyroxenite will also begin melting deeper than DC with the solidus-depth function derived by *Pertermann and Hirschmann* [2003]. The third component (EC) is assumed to be hydrous peridotite, to have a higher concentration of Sr and Nd relative to primitive mantle, and to have intermediate $^{87}Sr/^{86}Sr$ and $^{143}Nd/^{144}Nd$ isotope ratios. Because of the elevated water content, EC is assumed to begin melting deeper than DC and PC at a given temperature [e.g., *Katz et al.*, 2003]. Figure 7a shows the solidus-depth functions for the three different materials, an example mantle adiabat, T_a, and an example temperature profile, T, in the plume layer beneath the arch. The isotopic ratios, the Sr and Nd contents, and solidi of these

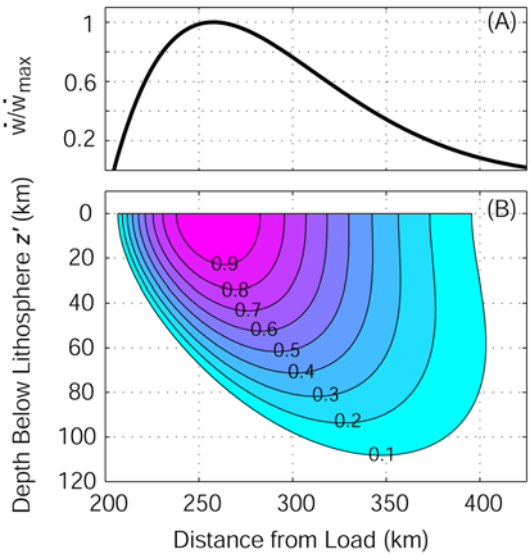

Figure 6. (a) Predicted rate of uplift of the flexural arch with elastic plate thickness T_e = 30 km. This curve is also the upper surface boundary condition on the asthenosphere derived from (2). (b) Contours of upwelling rate beneath the flexural arch normalized by the peak uplift at the arch. The flow solutions are from (14).

materials were chosen to represent the general characteristics of these materials; they must be specified to construct the reference models that we develop below, but, as we discuss later, the ability of the models to explain the geochemical observations are insensitive to the details of the above assumptions.

[24] Having defined the mantle components, we now examine their melting functions. Following *Ito and Mahoney* [2005], the extent of partial melting F and the melt productivity, $\partial F/\partial p$, are calculated using basic principles of phase equilibria and thermodynamics [*Hirschmann et al.*, 1999; *Phipps Morgan*, 2001]. The model assumes that the whole system is in thermal equilibrium, but the three components are chemically [*Phipps Morgan*, 2001; *Kogiso et al.*, 2004] and physically separated during melting and melt accumulation.

[25] Melting and melt accumulation are defined using the modal, dynamic melting equations described by *Albarède* [1995] and *Zou* [1998]. With this description, the mass fraction of melt extracted from the mantle X differs from F because a (small) mass fraction Φ of residual melt is retained in the matrix:

$$X = \frac{F - \Phi}{1 - \Phi} \quad \text{for } F \geq \Phi. \tag{16}$$

Taking the derivative of (16) with respect to pressure, p, yields the melt extraction productivity

$$\frac{\partial X}{\partial p} = \frac{\partial F}{\partial p}\frac{1}{1 - \Phi} \quad \text{for } F \geq \Phi. \tag{17}$$

Melt extraction productivity, $\partial X/\partial p$, is important because it determines the rate of melt extraction,

$$\frac{\partial X}{\partial t} = \frac{\partial X}{\partial p}\frac{dp}{dt}, \tag{18}$$

where the rate of total pressure change, dp/dt, = $\rho g v_z$ from (7). The productivity and rate of melt extraction are zero for $F \leq \Phi$, when the amount of melt is below the critical value Φ for melt to be extracted.

[26] As an example, Figure 7b shows a calculation of the melt extraction productivity functions for a plume layer fed by a mantle plume stem that started (i.e., prior to melting at the hot spot center) with a mean potential temperature of $\overline{T}_P$ = 1550°C. The results show that arch decompression will cause EC (hydrous peridotite) to melt (i.e., $\partial X^{EC}/\partial z = \rho g(\partial X^{EC}/\partial p) > 0$) throughout the plume layer.

Table 2. Assumed Component Compositions and Constants

	Depleted Component (DC)	Enriched Component (EC)	Pyroxenite Component (PC)
$^{143}Nd/^{144}Nd$	0.51307	0.51295	0.51259
$^{87}Sr/^{86}Sr$	0.70315	0.70370	0.70440

	Concentration in Anhydrous Peridotite (DC)[a,b]	Concentration in Enriched Peridotite (EC)[a,b]	Peridotite k_D	Concentration in Pyroxenite (PC)[a,b]	Pyroxenite k_D
Nd	0.74	1.28	0.0264	7.47	0.1500
Sr	0.59	1.57	0.0105	5.68	0.0678

[a] Element concentrations are normalized by the primitive mantle estimates of *Sun and McDonough* [1989].
[b] *Ito and Mahoney* [2005].

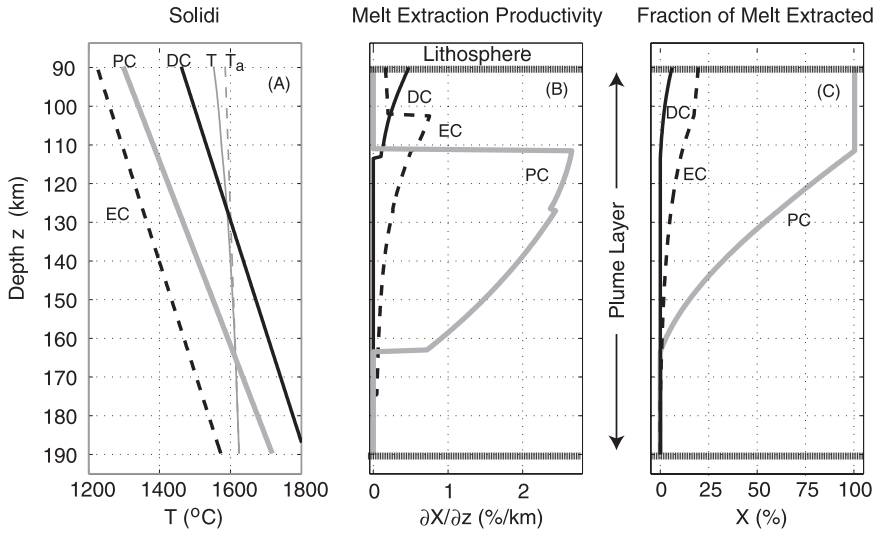

Figure 7. Melting functions based on *Ito and Mahoney* [2005]. The above curves show the properties in the asthenosphere beneath the arch that remain after melting at the hot spot center as a function of depth z. (a) Solidi of completely solid lithologic components: pyroxenite [*Pertermann and Hirschmann*, 2003] (PC, thick, solid gray), the hydrous, enriched peridotite (EC, black dashed), and the depleted component as anhydrous peridotite [*Hirschmann*, 2000] (DC, solid black). The adiabatic temperature profile (T_a, dashed gray) is for a plume potential temperature of 1550°C. The thin solid profile (T) shows the predicted temperature of the partially molten mantle; it deviates from T_a due to latent heat loss in melting a mantle mixture of ~90% DC, 5% EC, and 5% PC (deviation from T_a is computed by numerically integrating $(\partial T/\partial F)|_P \sum_{i=1}^{n} [\phi^i (\partial F^i/\partial P) dP]$, as done by *Ito and Mahoney* [2005]). (B) Melt extraction productivities for each component (as labeled) vary greatly with depth z. Here, we have imposed a 90-km-thick lithosphere and a 100-km-thick plume layer (i.e., melting can occur only between these depths). (C) The corresponding fraction of melt extraction as a function of depth z.

The extraction productivity for EC gradually increases with increasing extent of melting until dropping when clinopyroxene (cpx) is exhausted at $F = 0.18$ [e.g., *Asimow et al.*, 2001]. The melt extraction productivity function for DC is similar to that of EC in that it starts small and increases as pressure drops and F increases. The key differences are that the productivity of DC is lower than that of EC at the same F and DC productivity first becomes nonzero at shallower depths than EC (i.e., DC begins melting above EC). In this particular case, flexural decompression will cause DC to begin melting about halfway into the plume layer, and the plume layer is truncated by the base of the lithosphere before cpx is exhausted from DC. Pyroxenite (PC) is predicted to start melting near the bottom of the plume layer, and both $\partial X^{PC}/\partial z$ and X^{PC} are predicted to increase rapidly until PC is consumed (i.e., $F = 1$), in this case, at ~20 km below the base of the lithosphere.

[27] The amount that each component contributes to the volume and composition of the accumulated magma is determined by integrating melting rate of each component over the depth of the melting zone below a given point on the arch. The integral of melt production for component i (i.e., DC, EC, or PC) is

$$\dot{M}^i_{arch}(r) = \int_{z_1}^{z_2} \phi^i d\dot{M}^i_{arch} = \int_{z_1}^{z_2} \phi^i v_z(r, z') \frac{\partial X^i(z)}{\partial z} dz, \qquad (19)$$

where z is the depth below the seafloor at $r \to \infty$ (Figure 5), $d\dot{M}^i_{arch}$ is the rate of melting in each depth interval dz, ϕ^i is the starting mass fraction of the component in the solid mantle beneath the melting zone, z_2 is the depth at the base of the lithosphere, and z_1 is the depth at the base of the plume layer (Figure 5). It is important to note in (19) that melt extraction productivity depends on z, while vertical velocity depends on z'; both variables refer to depths far away from the arch ($r \to \infty$) and are simply related by $z = z' + z_2$.

[28] There are two important parameters that control (19), z_2 and $\overline{T}_P$. Varying z_2 affects the depths (or pressures) of (appreciable) upwelling $-v_z(r, z')$, while varying $\overline{T}_P$ affects the depths (or pressures) of appreciable productivity $\partial X^i(z)/\partial z$. For example,

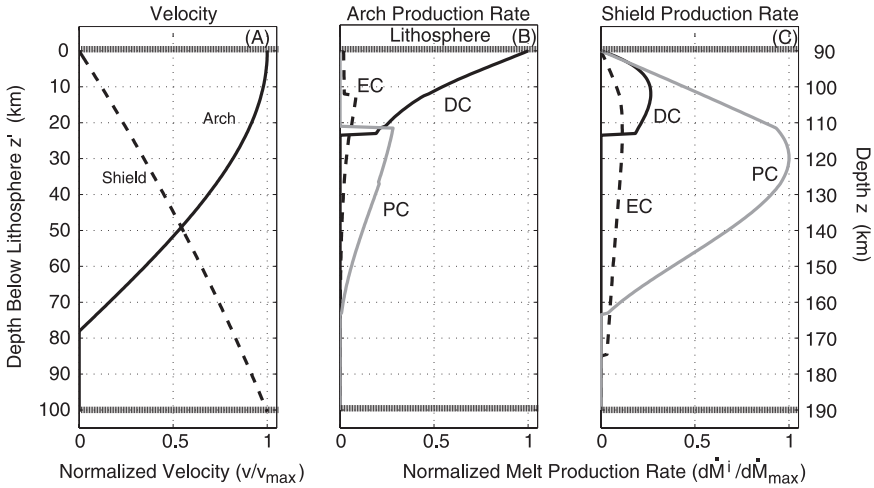

Figure 8. (a) Velocity profiles used to calculate melt production rate for the flexural arch (solid, from equation (14)) and the shield at the hot spot center (dashed, from equation (20)), normalized by their respective maxima, as a function of depth below the base of the lithosphere z' (at $r \rightarrow \infty$). For the arch melting zone, the vertical velocity $v_z(r, z')$ profile is shown at the radius where the arch uplifts the fastest (note that nonnormalized velocity under the arch is defined as negative). Lithospheric thickness z_2 = 90 km, plume thickness is 100 km, and mean plume potential temperature is 1550°C. (b) Incremental melt production rate at the arch as a function of depth z (the integrand of equation (19)) normalized by the maximum integrand of the DC production rate, for DC (solid black), EC (dashed black), and PC (solid gray) sources. In this example, $\phi^{DC} = 0.9$, $\phi^{EC} = 0.05$, and $\phi^{PC} = 0.05$. (c) Incremental melt production rate as a function of depth z (normalized by the maximum integrand of the PC production rate) predicted for melting beneath the hot spot center (the integrand of equation (21)) with the same starting mantle source composition as Figure 8b.

a thicker lithosphere moves the lithosphere/asthenosphere boundary to greater depth, and therefore the upwelling function $-v_z(r, z')$ shifts uniformly to a greater depth, while a higher plume potential temperature effectively shifts the extraction productivity function to a greater depth. Figure 8b illustrates an example calculation of how the incremental melt production rate (the integrand of equation (19)) varies as a function of depth for a lithospheric thickness of z_2 = 90 km and a mantle mixture of DC ($\phi^{DC} = 0.9$), EC ($\phi^{EC} = 0.05$), and PC ($\phi^{PC} = 0.05$). In this example, the zone of greatest DC productivity $\partial X^{DC}/\partial z$ (Figure 7b) and the zone of greatest upwelling (Figure 8a) are both near z = 90 km, whereas the zone of greatest productivities for EC and PC are ~15 km deeper where upwelling is slower (Figure 8a). The prediction of the zone of greatest DC productivity coinciding with the zone of greatest upwelling rate, this not being true for EC and PC, and the differences in mass fraction ϕ^i lead to greater area under the DC curve than under the EC and PC curves, or greater integrated melt production rate for DC, $\dot{M}^{DC}_{arch}$.

[29] The total integrated DC, EC, and PC melt production rates (19) for this same example depend on lithospheric thickness z_2, as shown in Figure 9a. Calculations predict DC to have a higher integrated production rate than EC or PC for lithospheric thickness between 50 and 95 km. Thus, for these lithospheric thicknesses, DC melts are predicted to dominate the total volume and composition of crust formed due to melting beneath the flexural arch.

3.4. Melting at the Hot Spot Center

[30] To address the different geochemical characteristics between secondary and shield volcanism, we must also produce a model for melting beneath the hot spot center. Following *Ito and Mahoney* [2005], we compute the melt production rate for the entire hot spot melting zone by considering the fraction of melt extracted as a function of depth $X(z)$, and the radial flow rate $v_r(z')$ of all of the residue leaving the melt zone. The radial velocity $v_r(z')$ can be simply described by the flow profile in an expanding gravity current. The solution is [*Huppert*, 1982, equation (2.7)]

$$v_r(z') \propto (z_1 - z_2)z' - z'^2, \tag{20}$$

where in this case, $v_r(z')$ is the radial velocity at the edge of the plume melting zone (i.e., where plume upwelling is zero; see *Ito and Mahoney* [2005] for further explanation), and therefore is not a function

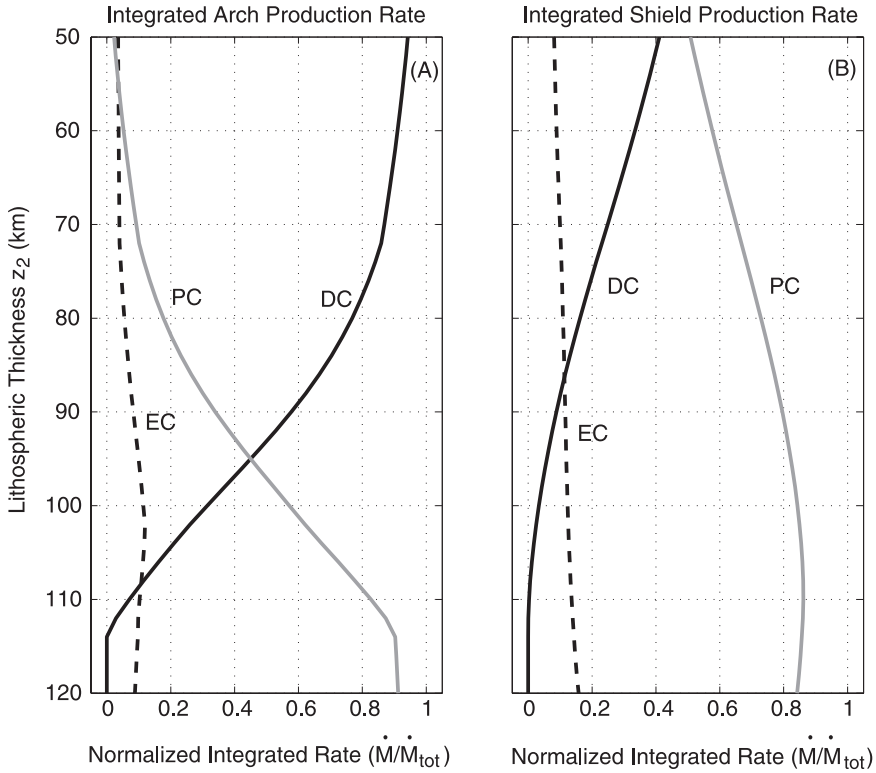

Figure 9. (a) Normalized integrated melt production rate under the flexural arch for the plume scenario as in Figure 8, for varying lithospheric thickness, z_2. DC (solid black), EC (dashed), and PC (solid gray) sources melt production rate is integrated over the thickness of the 100-km-thick plume layer. (b) Normalized integrated melt production rate calculated at the hot spot center. In both Figures 9a and 9b, $\phi^{DC} = 0.9$, $\phi^{EC} = 0.05$, and $\phi^{PC} = 0.05$.

of r. The radial flow rate $v_r(z')$ determines the rate at which residue with extracted melt fraction $X(z)$ is created by melting. The production rate of the whole melting zone from component i beneath the shield is thus

$$\dot{M}^i_{shield} = \int_{z_1}^{z_2} \phi^i v_r(z') X^i(z) dz. \tag{21}$$

[31] As before, we provide an example calculation of the incremental melt production rate as a function of depth (i.e., the integrand of equation (21)) in Figure 8c. Compared to melting beneath the arch, melting beneath the shield generates a significantly larger production rate of PC, a somewhat larger production rate of EC, and a smaller production rate of DC. The main reason is that the amount of mantle melting at a given depth (as measured by $v_r(z')$) increases quadratically with z'. This enhances melt extraction near the base of the melting zone, where EC and PC are dominantly melting, and diminishes melt extraction near the base of the (rigid) lithosphere, where DC is melting. Figure 9 shows the effect of changing lithospheric thickness on total melt production rate, $\dot{M}^i_{shield}$. In this example (and for $z_2 > 50$ km) PC dominates the contribution to the total crustal volume and geochemistry calculated for shield magmas.

3.5. Efficiency of Crustal Production by Flexural Arch Decompression

[32] One way to relate our calculations to observations is to compute the thickness of lava predicted if all the melt in our model mantle erupted. In order to compute the thickness of lava formed at the arch, the melt production rate is converted to melt thickening rate using the following equation:

$$\dot{h}^i_{cr}(r) = \frac{\rho_{mantle}}{\rho_L} \dot{M}^i_{arch}. \tag{22}$$

Here $\dot{h}^i_{cr}(r)$ is the rate at which a layer of lava would thicken if all the magma at a radius r rises vertically in the mantle to the surface. It is essentially the magma volume flux per unit area of seafloor. We evaluate (19) and (22) for all radial distances over which arch uplift rate is positive, r_+.

Table 3. Mineral Proportions and Element Partition Coefficients

	Olivine	Orthopyroxene	Clinopyroxene	Garnet
Proportions in peridotite[a,b]	0.598	0.211	0.076	0.115
Proportions in pyroxenite[c,d]	0.0	0.04	0.78	0.18
Coefficients for Nd[e]	4.2 E-4	0.0012	0.19	0.10
Coefficients for Sr[e]	0.0015	5.1 E-4	0.08	0.03

[a] *McKenzie and O'Nions* [1991].
[b] *Green* [2000].
[c] *Hirschmann and Stolper* [1996].
[d] *Pertermann and Hirschmann* [2003].
[e] *Green* [1994].

The maximum thickening rate occurs at the radius of maximum rate of uplift. The average magma thickening for all lithologies over the whole arch melting zone is normalized by the maximum uplift of the arch, $w_{\max}$, to yield the average thickening rate per unit uplift

$$\dot{\bar{H}}_{cr} = \frac{\sum_{i}^{n} \int_{r_+} \dot{h}^i_{cr} dr}{r_+ w_{\max}}, \tag{23}$$

where $n = 3$. We use results from (23) in subsequent calculations to compare predicted and observed rates of secondary volcanic crustal formation.

4. Magma Compositions

[33] To solve for the Nd- and Sr-isotopic composition of magmas produced at the hot spot and beneath the flexing arch, we must first compute the concentrations of these elements in the magmas. The concentration of Nd and Sr in the melt is proportional to the amount these incompatible elements are enriched in the melt compared to the starting solid. At the arch, the appropriate enrichment function (for lithology i) is the modal, dynamic melting function [*Albarède*, 1995; *Zou*, 1998]

$$E^i_{arch}(z) = \frac{(1 - X^i)^{[1/(\Phi+(1-\Phi)k_D)]-1}}{\Phi + (1-\Phi)k_D}. \tag{24}$$

Here $E^i_{arch}(z)$ is the concentration of Nd or Sr in the incremental melt (for the arch melting zone) normalized by the concentration in the starting, unmelted solid C^i_o (see Table 2) for component i, and k_D is the bulk distribution coefficient for the particular element (see Tables 2 and 3). This "incremental" melt enrichment function allows us to compute the composition of melts extracted everywhere beneath the arch, and then integrate over depth to predict the composition of secondary lavas. In contrast at the hot spot center, the enrichment function is [*Albarède*, 1995; *Zou*, 1998]

$$E^i_{shield}(z) = \frac{1}{X^i}\left[1 - \left(1 - X^i\right)^{[1/(\Phi+(1-\Phi)k_D)]}\right]. \tag{25}$$

This function describes the enrichment of "integrated" dynamic melts and is appropriate for computing the mean composition of melts integrated over the whole hot spot melting zone. Note, although we are assuming modal melting in computing enrichment functions ($E^i(z)$) but include a change in mineralogy due to the loss in cpx in our computation of $\partial X/\partial p$ versus pressure (equation (17)), equations (24) and (25) are reasonable approximations because the solutions are insensitive to changes in k_D for $F \gg k_D$ where cpx exhaustion occurs.

[34] The average concentration of the element in the melt, C^i_L, is the average of the product of $E^i(z)$ ((24) for arch melting and (25) for shield magmatism) and C^i_o weighted by the melt production rate at each depth [*Albarède*, 1995]

$$C^i_L = C^i_o \left[\frac{\int_{z_1}^{z_2} E^i(z) \frac{\partial \dot{M}^i}{\partial z} dz}{\dot{M}^i}\right], \tag{26}$$

where $\partial \dot{M}^i/\partial z$ is the incremental melt production rate or the integrand of (19) or (21). The total isotopic ratio in the final mixture, I^τ, is the weighted average

$$I^\tau = \frac{\sum_{i}^{n} I^i_o C^i_L \dot{M}^i}{\sum_{i}^{n} C^i_L \dot{M}^i}, \tag{27}$$

where I_o^i is the mean isotopic ratio in component i (see Table 2 and Figure 3).

[35] Finally, we calculate mean extent of partial melting, which is relevant to the major-element properties of the melt. The appropriate calculation is F_v as discussed by *Plank et al.* [1995]. For a single component and for $F^i(z) \geq \Phi$

$$F_v^i = \left[\frac{\int_{z_1}^{z_2} F^i(z) \frac{\partial \dot{M}^i}{\partial z} dz}{\dot{M}^i} \right]. \quad (28)$$

For depths where $F^i(z) \leq \Phi$, $F_v^i = 0$. The total F_v is the weighted average of the contributions from each component,

$$F_v = f^i \left[\frac{\sum_i^n F_v^i \dot{M}^i}{\sum_i^n \dot{M}^i} \right]. \quad (29)$$

The factor f^i has been adopted to relate the extents of partial melting for pyroxenite to that of peridotite [*Ito and Mahoney*, 2005]. For the DC and EC components, $f^i = 1$, since they are both peridotite. For the PC component, we assume, $f^{PX} = 0.15$, which implies that 100% melting of PC will yield melts of the same composition as 15% melting of peridotite.

5. Results of Modeling

5.1. Efficiency of Magma Production Due to Flexural Arch Decompression

[36] Many parameters control the amount and composition of crust in this model of flexural decompression. For simplicity, we report results with respect to three critical parameters: the relative fraction of each component in the mantle ϕ^i, lithospheric thickness, z_2, and mean plume temperature $\overline{T}_P$. In all scenarios $\Phi = 0.01$ [*Sims et al.*, 1999; *Pietruszka et al.*, 2001]. Results are shown for two example sources arbitrarily chosen, but with the assumption that the plume will be predominantly DC. Case 1 is a plume where $\phi^{EC} = 0.05$, $\phi^{PC} = 0.05$, and $\phi^{DC} = 0.9$. In Case 2, $\phi^{EC} = 0.095$, $\phi^{PC} = 0.005$ and $\phi^{DC} = 0.9$.

[37] The predicted rate of magmatic crustal formation per meter of maximum uplift (i.e., the efficiency of magma production), $\dot{\overline{H}}_{cr}$ (23) for the two example cases depends on lithospheric thickness z_2 and mean plume potential temperature $\overline{T}_P$ (Figure 10). Both cases predict the same general pattern. For cooler plumes and thick lithosphere, $\dot{\overline{H}}_{cr}$ is low. This occurs because at low $\overline{T}_P$ and large z_2, melting is restricted to a zone near or below the solidus of DC, and near the solidus of EC and PC, where $\partial X^{EC}/dz$ and $\partial X^{PC}/dz$ are low (see equation (19)). Increasing $\overline{T}_P$ and decreasing z_2 results in larger magma production efficiencies as the height of the melting zone and $\partial X^i/\partial z$ increase. But at a certain limit, at high $\overline{T}_P$ and low z_2, $\dot{\overline{H}}_{cr}$ begins to decline because $\partial X^i/\partial z$ are again low because cpx has been exhausted from peridotite (DC and EC) and pyroxenite (PC) has been consumed. For our reference plume temperature of $\overline{T}_P = 1550°C$ the most efficient rate of magma production for Case 1 of 0.098 m/m_{uplift} s^{-1} occurs for $z_2 = 64$ km. For Case 2, the most efficient melting is 0.097 m/m_{uplift} with thinner lithosphere, $z_2 = 58$ km.

5.2. Difference in Isotope Compositions Between Secondary and Shield Lavas

[38] We now compare predicted and observed $^{143}Nd/^{144}Nd$ and $^{87}Sr/^{86}Sr$ isotope compositions for the secondary (arch) and shield (hot spot center) lavas. The observed ratios are characterized on the basis of the mean and one standard-deviation variation of data for secondary Hawaiian lavas [*Okano and Tatsumoto*, 1996; *Reiners and Nelson*, 1998; *Lassiter et al.*, 2000; *Frey et al.*, 2000] and Hawaiian shield lavas (GEOROC database, http://georoc.mpch-mainz.gwdg.de): $I^{Nd}_{secondary} = 0.51304 \pm 3.5 \cdot 10^{-5}$, $I^{Sr}_{secondary} = 0.70326 \pm 1.03 \cdot 10^{-4}$, $I^{Nd}_{shield} = 0.51292 \pm 7.5 \cdot 10^{-5}$, and $I^{Sr}_{shield} = 0.70372 \pm 1.85 \cdot 10^{-4}$ (Figure 3).

[39] The theoretical values of $^{143}Nd/^{144}Nd$ and $^{87}Sr/^{86}Sr$ (equation (27)) within one standard deviation of the corresponding observation for the arch and shield lavas are shown in Figure 11. In all of these results, contours of isotope ratios are diagonal (in $\overline{T}_P - z_2$ space) with predicted $^{143}Nd/^{144}Nd$ generally increasing and $^{87}Sr/^{86}Sr$ generally decreasing with decreasing lithospheric thickness and increasing mean temperature. At low temperatures, thick lithosphere, or both, $^{143}Nd/^{144}Nd$ is predicted to be low and $^{87}Sr/^{86}Sr$ is predicted to be high because PC and EC contribute mostly to the melt (e.g., Figure 9 illustrates this effect with respect to increasing lithospheric thickness for a single temperature). Likewise at high temperatures, thin lithosphere, or both, $^{143}Nd/^{144}Nd$ is predicted to be high and

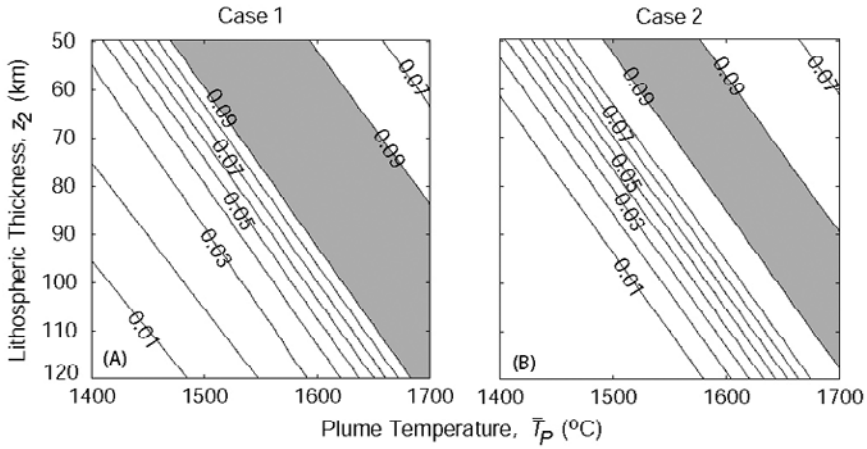

Figure 10. Average magma thickening rate $\dot{\overline{H}}_{cr}$ (equation (23)) formed from flexural decompression under the arch as a function of lithospheric thickness and plume temperature. Gray bands show temperature and depth ranges with maximum $\dot{\overline{H}}_{cr}$. (a) For Case 1: $\phi^{DC}|[\phi^{EC}|\phi^{PC} = 0.9|0.05|0.05$. (b) For Case 2: $\phi^{DC}|\phi^{EC}|\phi^{PC} = 0.9|0.095|0.005$.

$^{87}Sr/^{86}Sr$ is predicted to be low because at these conditions DC is mostly contributing to the melt. Other calculations (not shown) indicate that increasing ϕ^{EC} or ϕ^{PC} relative to ϕ^{DC} has the effect of shifting the contours of predicted isotope ratio to higher temperatures or to thinner lithospheres.

[40] The successful source composition will predict the observed mean Nd- and Sr-isotope ratios for both the secondary and shield lavas with a common range of $\overline{T}_P$ and z_2. For Case 1 (Figures 11a, 11b, 11c, 11d), a range of common plume temperatures and lithospheric thicknesses successfully yield the observed mean $^{87}Sr/^{86}Sr$ and $^{143}Nd/^{144}Nd$ composition for the secondary lavas. However, a different range of $\overline{T}_P$ and z_2 yields agreement with the range defined for shield lavas. Case 1 therefore fails our test. In Case 2 (Figures 11e, 11f, 11g, 11h), we predict the mean $^{87}Sr/^{86}Sr$ and $^{143}Nd/^{144}Nd$ for both secondary and shield lavas within the constraints of observed data with a range of $\overline{T}_P$ and z_2 common to all four of the calculations. For our reference temperature of 1550°C, the successful range of lithospheric thickness is 92 km < z_2 < 98 km.

5.3. Mean Extent of Melting

[41] To address the major-element differences between the secondary and shield lavas, we now examine the mean extent of melting predicted by arch decompression and by melting at the hot spot center. Figure 12 shows the calculated mean extent of melting for the plume source scenarios. We now focus on the remaining plume source scenario (Case 2; Figure 12b) that can match observed values of I^{Nd}_{arch}, I^{Nd}_{shield}, I^{Sr}_{arch}, and I^{Sr}_{shield}. This plot compares the mean extent of melting at the arch and at the plume stem for the reference temperature of $\overline{T}_P$ = 1550°C. Mean extent of melting for the shield F_v^{shield} exceeds that for the arch F_v^{arch} for lithospheric thicknesses of z_2 = 80 to 104 km. This range of z_2 includes the thickness range z_2 = 92–98 km that yielded successful matches to the isotope data for the secondary and shield lavas. At z_2 = 92 km, $F_v^{shield} - F_v^{arch}$ is ~1.42%; at z_2 = 98 km, $F_v^{shield} - F_v^{arch}$ = ~1.11%. In fact, we find that $F_v^{shield} > F_v^{arch}$ for a range of lithospheric thicknesses that yield successful matches to the observed isotope variations for a wide range of temperatures ($\overline{T}_P$ = 1400 to 1700°C).

[42] For comparison, the predicted profiles of mean extent of partial melting F_v for Case 1 shows a less restricted lithospheric thickness range where $F_v^{shield} > F_v^{arch}$. Also, $F_v^{shield} - F_v^{arch}$ is typically larger for Case 1 compared to Case 2. Although there is the isotope discrepancy with regards to Case 1, this prediction emphasizes the importance of pyroxenite in the assumed mantle composition. Prior calculation without pyroxenite (not shown) predicted that differences between F_v^{shield} and F_v^{arch} are negligible, and therefore differences in major-element composition of magmas are assumed negligible. The remaining successful mantle component model is Case 2, although we stress that it is not a unique solution.

6. Discussion

[43] The model of flexure-induced magmatism successfully predicts many general aspects of four observations of secondary volcanism of the Ha-

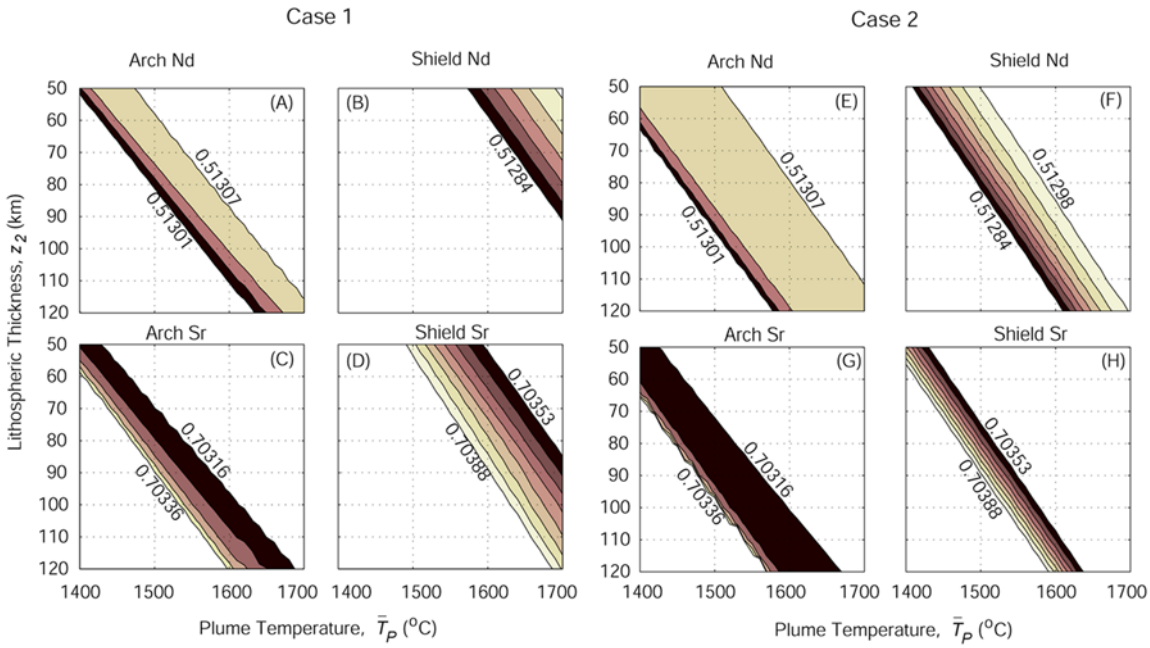

Figure 11. Predicted isotopic value (equation (27)) as a function of lithospheric thickness and plume temperature. Contours show values inside the observed range for Hawaiian lava. White regions fall outside the observed range and are therefore rejected. (a–d) Case 1: $\phi^{DC}|\phi^{EC}|\phi^{PC} = 0.9|0.05|0.05$. (a and b) The Nd isotope ratio computed for the arch and shield, respectively, with contour intervals of 10^{-5}. (c and d) The Sr isotope ratio computed for the arch and shield, respectively, with contour intervals of 10^{-5}. (e–h) The same as Figures 11a–11d except for Case 2: $\phi^{DC}|\phi^{EC}|\phi^{PC} = 0.9|0.095|0.005$.

waiian Islands. Specifically, the flexure model predicts the appropriate temporal and spatial separation between the active shield and secondary volcanism for a realistic lithospheric thickness range. Melting by flexural arch decompression also can yield the appropriate difference in Sr and Nd isotopes between shield and secondary lavas, and lead to lower mean extents of melting beneath arch compared to melting beneath the shield. We now discuss the volume of melt produced, explore some further implications of the flexure model, and present shortcomings that require further study.

6.1. Observed and Calculated Crustal Formation

[44] *Walker* [1990] estimated an average melt flux of ~20 km^3/Myr for Honolulu rejuvenation volcanism. The most efficient crustal production rate predicted for our successful model conditions (Case 2, with lithospheric thicknesses (z_2) that produce successful isotope predictions and $F_v^{shield} > F_v^{arch}$) is 0.042 m/m$_{uplift}$. To estimate absolute crustal thickness, we need constraints on arch uplift. Geophysical studies infer a ~5 km downward deflection of the seafloor beneath Oahu [*Watts et al.*, 1985; *Watts and ten Brink*, 1989], for which the flexure calculation would predict ~75 m of uplift at the flexural arch of Oahu (equation (2)). This value, however, may be a lower bound because erosion and mass wasting has significantly reduced (>40%) the original load of Oahu [*Smith and Wessel*, 2000; *Satake et al.*, 2002]. Indeed, geologic evidence suggests Lanai, Molokai and Oahu may have uplifted (as this work assumes, due to loading associated with volcanism on Hawaii) by ~100 m [*Stearns*, 1978; *Jones*, 1993; *Grigg and Jones*, 1997]. Assuming a total uplift of 100 m and that it occurs over one million years, our model predicts an average crustal production rate of 4.2 m/Myr. In order to generate the estimated volume flux of 20 km^3/Myr, secondary eruptions of Honolulu would have to draw magma from the decompressing mantle below an area of ~4760 km^2 (approximately equivalent to a circular area of radius 39 km). Our model does not include a melt focusing mechanism, but one may exist. For example, volcanic loading could align the maximum principal stress in the lithosphere, such that magma propagates in dikes to the volcano from regions much larger than the eruption area [*ten Brink and Brocher*, 1987; *Hieronymus and Bercovici*, 1999, 2001; *Muller et al.*, 2001]. More precise measurement of the flux of onshore secondary volcanism would allow for better estimates of the area from which such focusing occurs.

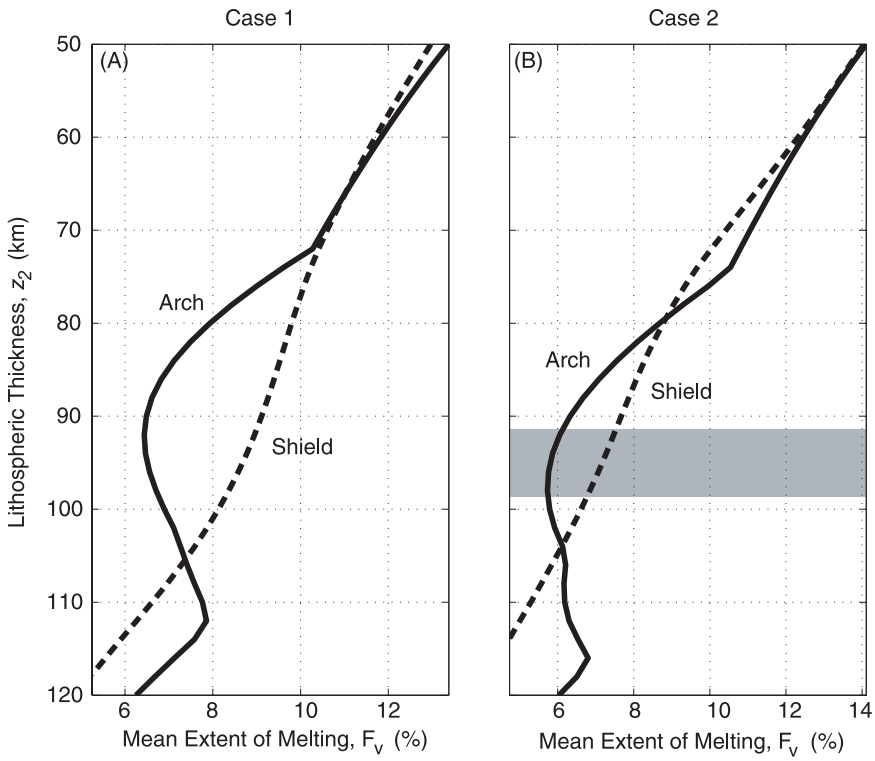

Figure 12. Mean extent of partial melting for $\overline{T}_P$ = 1550°C plume as a function of lithospheric thickness (equation (29)). (a) F_v in Case 1 $\phi^{DC}|\phi^{EC}|\phi^{PC} = 0.9|0.05|0.05$, for arch (solid) and shield (dashed) magmas. (b) As in Figure 12a for the Case 2 plume where $\phi^{DC}|\phi^{EC}|\phi^{PC} = 0.9|0.095|0.005$. Gray band marks thicknesses for which models successfully predict the observed mean isotope compositions (see Figures 11e, 11f, 11g, and 11h).

[45] On the basis of bathymetric surveys that covered about one-third of the North Arch field and submersible surveys of at least one pit crater (122 m deep), the average thickness of the at the North Arch volcanic lava has been estimated by *Clague et al.* [2002] to be ~40–50 m. These thicknesses are an order of magnitude greater than the total thickness predicted from our preferred model. Perhaps some magma focusing occurs from a broader region in the mantle to thicken the crust of the North Arch field. Another explanation is that while our simple model addresses the flexure caused by the growth of only a single shield volcano, in reality, multiple shields grow at the same time. Coeval shield loading could have caused a greater flexural uplift and likewise, more melting, along and away from the island chain than predicted by our model. For example, load groups such as West Maui, Lanai, and East and West Molokai, or the volcanoes on Hawaii could combine to increase deflection at the North and South Arch (Figure 2). Multiple load geometry is also a method to get offshore secondary volcanism over distances and areas larger than the predicted uplift for a single load (Figures 1 and 4). We note that to test or further constrain this model, improved constraints on offshore as well as onshore eruption volumes are needed.

6.2. Mean Extent of Melting and Major Elements

[46] A very simple attempt is made to address differences in major-element compositions between shield and secondary volcanism by computing mean extent of partial melting. We cannot yet address how low F_v^{arch} must be to yield the appropriate compositions. Thus far, the model produces a difference in F_v between secondary and shield lavas in the rights sense, i.e., $F_v^{shield} > F_v^{arch}$. The precise values of F_v^{shield} and F_v^{arch} depend on the rather crude correction factor, f^i, and the use of F_v^{shield} and F_v^{arch} to infer differences in major elements can only be qualitative. Clearly future efforts are necessary to explicitly compute major-element compositions as a function of source composition, pressure of melting, volatile content, as well as F [e.g., *Asimow et al.*, 2004], to test whether flexural decompression of a heterogeneous mantle can indeed generate alkalic secondary lavas [*Macdonald and Katsura*, 1964]. These future efforts must consider the physical and chemical conditions.

6.3. Isotopic Variation

[47] Our quantitative method requires that we define specific isotopic compositions of each mantle source component and we put forth one, nonunique solution. This solution is not meant to constrain the composition of the mantle, but rather illustrates one set of conditions for which the flexure model works. We have found models with other starting conditions to work equally well, such as models with slightly different isotopic compositions for the different components, or models that trade isotopic compositions between the PC and EC components. Showing all of these possible solutions would be tiresome, but what they reveal is that the flexure model we forward is relatively insensitive to many details of the starting heterogeneous source. However, the models do require two main conditions of the source: EC and PC must begin melting deeper than DC and PC must be present.

[48] The condition that EC and PC begin melting deeper than DC is required as a consequence of our consideration of the melting processes and is similarly noted in other work [*Hirschmann and Stolper*, 1996]. We find that at the plume center, more starting material moves through the base of the melting zone than at the top, thus the plume melting zone more heavily samples deep melting lithologies. Therefore our model predicts what has long been recognized in that Hawaiian shield volcanism is dominated by enriched components. What is different here from other studies is that by considering the melting processes, we predict the mixture in the melt to differ substantially from the mixture in the starting material. Also, we predict the shield and arch melting zones to yield very different melt compositions from the same starting mantle source. This illustrates the importance of considering the melting processes in further interpretations relating magma to the source.

[49] The condition that PC be present in the mantle allows for our models to predict lower mean extents of melting for rejuvenated volcanism compared to shield volcanism. Pyroxenite has indeed been suggested to be an important component for both the Hawaiian shield [*Hauri*, 1996; *Hauri et al.*, 1996] and rejuvenated lavas [*Lassiter et al.*, 2000; *Yang et al.*, 2003], and may be important in other ocean-island basalts [*Hirschmann et al.*, 2003]. A possible weakness of our model, however, comes from osmium isotope data. On one hand, both the shield and rejuvenated lavas show evidence for a high $^{187}Os/^{188}Os$ source, which has been interpreted to be pyroxenite [*Hauri*, 1996; *Hauri et al.*, 1996; *Lassiter and Hauri*, 1998; *Lassiter et al.*, 2000; *Yang et al.*, 2003]. On the other hand, the high $^{187}Os/^{188}Os$ source for the shield and rejuvenated lavas appear to have distinct Sr and Nd isotope compositions, which does not support a single pyroxenite source as we have modeled. One possibility is that rejuvenated lavas are fed by pyroxenite melts from the lithosphere [*Lassiter et al.*, 2000; *Yang et al.*, 2003], which our models do not consider. Alternatively, if both high $^{187}Os/^{188}Os$ (and by inference pyroxenite) sources are present in the plume layer, then there must be some mechanism causing one source to be extracted more heavily beneath the shield while the other source to be more heavily melted beneath the arch. This would likely require the two (pyroxenite) sources to have different melting behaviors and this should be the topic of future testing.

6.4. Validity of the Physical Properties of the Mantle

[50] This work presents a reference model that agrees well with isotopic data and mean extent of partial melting data, and predicts significant crust formation, all with lithospheric thicknesses of $\sim$92–98 km for an average plume temperature of 1550°C. The above range of lithospheric thicknesses is consistent with that expected for 90-Myr-old oceanic lithosphere, according to a plate-cooling model [e.g., *Turcotte and Schubert*, 2002] and is consistent with constraints provided by seismic studies around Hawaii [*Woods et al.*, 1991; *Woods and Okal*, 1996]. Lower plume temperatures would require a thinner lithosphere to explain the data, which would be in agreement with other seismic data [e.g., *Bock*, 1991; *Priestley and Tilmann*, 1999; *Li et al.*, 2000]. Furthermore, the reference mean plume potential temperature of 1550°C is similar to that constrained by geodynamic studies of swell formation and crustal production [e.g., *Ribe and Christensen*, 1999]. The reference model thus explains, to varying degrees of success, all four of the general observations of secondary volcanism with reasonable values of lithospheric thickness and mean plume temperature.

[51] A final parameter worth further discussion is plume layer thickness. In the calculations shown, the layer of hot plume material downstream of the lithosphere ($z_2 - z_1$) is assumed to be 100 km. This work does not explore cases with different plume layer thickness, but we have evaluated some general effects. Thinner layers tend to reduce the amount of crust generated, while thicker layers

increase crustal production. Different layer thicknesses require different values of z_2 and $\overline{T}_P$ to explain the isotope differences and apparent low F_v for secondary lava compared to shields. The only existing seismic constraints on the thickness of a plume layer anywhere, suggests a thickness of the Iceland plume layer of $\leq$200 km [*Allen et al.*, 2002]. Future seismological studies to better constrain the thickness of the hypothesized Hawaiian plume layer will be valuable in further constraining or testing the flexure model.

7. Conclusions

[52] Secondary volcanism at Hawaii is manifested in two forms: onshore rejuvenated eruptions and the Hawaiian Arch eruptions. This paper proposes a model in which both types of volcanism originate as a direct consequence of flexural uplift, which surrounds new volcanic shields as they grow. The uplift causes decompression of the underlying heterogeneous mantle plume material, which first melted partially beneath the shield, but has since flowed laterally and is now beneath the arch. In support of this model, we have shown that secondary volcanism frequently occurs at locations predicted for the rising flexural arch of active volcanic shields. The predicted magma volume fluxes are comparable to crustal production rates of onshore and offshore secondary volcanism, if magma focuses from broad areas in the mantle to individual eruptions sites. The model successfully predicts Nd and Sr isotope observations for a range of lithospheric thickness and plume temperatures, with a mixture of a depleted peridotite source and an enriched pyroxenite source. The same parameters also predict mean extents of partial melting that are consistent with alkalic magma generated beneath the arch and tholeiitic magma generated in the plume stem. The most important model parameters are lithospheric thickness and mean mantle temperature. The reference values of these two parameters are consistent with constraints from geophysical studies. The main strength of the model is that it is able to predict many of the first order features of secondary volcanism.

Appendix A: Solution for Flow of the Asthenosphere

[53] To obtain solutions for the asthenospheric model, we define the Hankel transform pair of order ν according to

$$\hat{f}(\xi,z') = \int_0^\infty f(r,z')J_\nu(\xi r)rdr,$$
$$f(r,z') = \int_0^\infty \hat{f}(\xi,z')J_\nu(\xi r)\xi d\xi. \tag{A1}$$

The first-order Hankel transform of (10) yields

$$\left(\frac{d^2}{dz^2} - \xi^2\right)^2 \hat{\Psi}(\xi,z') = 0, \tag{A2}$$

where $\Psi = \psi/r$ and

$$\hat{\Psi}(\xi,z') = \int_0^\infty \Psi(r,z')J_1(\xi r)rdr. \tag{A3}$$

Solving (A2) we obtain

$$\hat{\Psi}(\xi,z') = (A(\xi) + B(\xi)z')e^{-\xi z'} + (C(\xi) + D(\xi)z')e^{\xi z'}. \tag{A4}$$

For vanishing velocities as $z' \rightarrow \infty$, $C = D = 0$. The remaining two coefficient functions are determined from the boundary conditions (11) and (12) in ξ space. Taking the zeroth-order Hankel transform of (11) and the first-order Hankel transform of (12) we obtain

$$v_z(\xi,z') = \xi\hat{\Psi} = \dot{w}(\xi), \quad z' = 0,$$
$$v_r(\xi,z') = -\frac{d\hat{\Psi}}{dz} = 0, \quad z' = 0, \tag{A5}$$

respectively, where $\dot{w}(\xi)$ is given by (B4) (see Appendix B). Substituting (A4) into (A5) and invoking (B4), we obtain

$$\xi A = B = \dot{w}(\xi) = \frac{\dot{Q}}{2\pi\Delta\rho g}\left[\frac{1}{1+(\alpha\xi)^4}\right]; \tag{A6}$$

hence

$$v_z(\xi,z') = \xi\hat{\Psi} = \dot{w}(\xi)(1+\xi z')e^{-\xi z'}. \tag{A7}$$

Inverting the Hankel transform of (A7) yields the vertical velocity

$$v_z(r,z') = \frac{\dot{Q}}{2\pi\Delta\rho g}\int \frac{1+\xi z'}{1+(\alpha\xi)^4}e^{-\xi z'}J_0(\xi r)\xi d\xi. \tag{A8}$$

A numerical approximation to (A8) using the trapezoid rule is given in (14).

Appendix B: Hankel Transform of the Surface Boundary Condition

[54] In order to apply the rate of flexure as a boundary condition on the asthenosphere model,

the Hankel transform of the vertical displacement rate, $\dot{w}$, must be obtained. Nadai's solution, (2), is not readily transformed, thus we formulate and solve for $\dot{w}$ using Hankel transforms.

[55] Here we solve the time-derivative of (1) subject to [*Nadai*, 1931] (where a dot above a variable indicates a time-derivative)

$$\begin{aligned} \dot{w}(r) &\to 0, \quad r \to \infty \\ |\dot{w}(r)| &< \infty, \quad r = 0 \end{aligned} \tag{B1}$$

and

$$\begin{aligned} \frac{d\dot{w}(r)}{dr} &= 0, \quad r = 0 \\ \frac{d\nabla^2\dot{w}(r)}{dr} &= \frac{\dot{Q}}{2\pi D r}, \quad r = 0. \end{aligned} \tag{B2}$$

[56] Taking the zeroth-order Hankel transform of the time derivative of (1) subject to (B1) and (B2), we obtain

$$\left[\frac{\Delta\rho g}{D} + \xi^4\right]\dot{w}(\xi) = \frac{\dot{Q}}{2\pi D}, \tag{B3}$$

which yields the required Hankel transform of the rate of vertical displacement applied in (A6),

$$\dot{w}(\xi) = \frac{\dot{Q}}{2\pi\Delta\rho g}\left[\frac{1}{1 + (\alpha\xi)^4}\right], \tag{B4}$$

where $\alpha = \left(\frac{D}{\Delta\rho g}\right)^{\frac{1}{4}}$.

Acknowledgments

[57] Bianco and Ito were supported by NSF-OCE02-21889 and Ito's new faculty startup from SOEST. This work was greatly improved by discussions with Pål Wessel and constructive revisions by Uri ten Brink, Paul Asimow, and editor William White. This is SOEST contribution 6598.

References

Albarède, F. (1995), *Introduction to Geochemical Modeling*, 543 pp., Cambridge Univ. Press, New York.

Allen, R. M., et al. (2002), Imaging the mantle beneath Iceland using integrated seismological techniques, *J. Geophys. Res.*, *107*(B12), 2325, doi:10.1029/2001JB000595.

Asimow, P. D., M. M. Hirschmann, and E. M. Stolper (2001), Calculation of peridotite partial melting from thermodynamic models of minerals and melt, IV. Adiabatic decompression and the composition and mean properties of mid-ocean ridge basalts, *J. Petrol.*, *42*(5), 963–998.

Asimow, P. D., J. E. Dixon, and C. H. Langmuir (2004), A hydrous melting and fractionation model for mid-ocean ridge basalts: Application to the Mid-Atlantic Ridge near the Azores, *Geochem. Geophys. Geosyst.*, *5*, Q01E16, doi:10.1029/2003GC000568.

Bock, G. (1991), Long-period S to P converted waves and the onset of partial melting beneath Oahu, Hawaii, *Geophys. Res. Lett.*, *18*, 869–872.

Chen, C.-Y., and F. A. Frey (1983), Origin of Hawaii tholeiite and alkalic basalt, *Nature*, *302*(28), 785–789.

Chen, C.-Y., and F. A. Frey (1985), Trace element and isotopic geochemistry of lavas from Haleakala Volcano, East Maui, Hawaii, *J. Geophys. Res.*, *90*(B10), 8743–8768.

Clague, D. A., and G. B. Dalrymple (1987), The Hawaiian-Emperor Volcanic Chain, *U.S. Geol. Surv. Prof. Pap.*, *1350*, 5–54.

Clague, D. A., and G. B. Dalrymple (1988), Age and petrology of alkalic postshield and rejuvenated stage lava from Kauai, Hawaii, *Contrib. Mineral. Petrol.*, *99*, 202–218.

Clague, D. A., and F. A. Frey (1982), Petrology and trace element geochemistry of Honolulu volcanics, Oahu: Implications for the oceanic mantle below Hawaii, *J. Petrol.*, *23*, 447–504.

Clague, D. A., R. T. Holcomb, J. M. Sinton, R. S. Detrick, and M. E. Torresan (1990), Pliocene and Pleistocene alkalic flood basalts on the seafloor north of the Hawaiian Islands, *Earth Planet. Sci. Lett.*, *98*, 175–191.

Clague, D. A., K. Uto, K. Satake, and A. S. Davis (2002), Eruption style and flow emplacement in the submarine North Arch Volcanic Field, Hawaii, in *Hawaiian Volcanoes: Deep Underwater Perspective*, *Geophys. Monogr. Ser.*, vol. 128, edited by E. Takahashi et al., pp. 65–84, AGU, Washington, D. C.

Crough, S. T. (1978), Thermal origin of mid-plate hotspot swells, *Geophys. J. R. Astron. Soc.*, *55*, 451–469.

DePaolo, D., and E. M. Stolper (1996), Models of Hawaiian volcano growth and plume structure: Implications of results from the Hawaii Scientific Drilling Project, *J. Geophys. Res.*, *101*(B5), 11,643–11,654.

Detrick, R. S., and S. T. Crough (1978), Island subsidence, hot spots, and lithospheric thinning, *J. Geophys. Res.*, *83*(B3), 1236–1244.

Dixon, J. E., D. A. Clague, P. Wallace, and R. Poreda (1997), Volatiles in alkalic basalts from the North Arch Volcanic Field, Hawaii, *J. Petrol.*, *38*(7), 911–939.

Frey, F. A., and J. M. Rhodes (1993), Intershield geochemical differences among Hawaiian volcanoes, *Philos. Trans. R. Soc. London, Ser. A*, *342*, 121–136.

Frey, F. A., M. O. Garcia, W. S. Wise, A. Kennedy, P. Gurriet, and F. Albarede (1991), The evolution of Mauna Kea Volcano, Hawaii: Petrogenesis of tholeittic and alkalic basalts, *J. Geophys. Res.*, *96*(B9), 14,347–14,375.

Frey, F. A., D. A. Clague, J. J. Mahoney, and J. M. Sinton (2000), Volcanism at the edge of the Hawaiian plume, *J. Petrol.*, *44*(5), 667–691.

Frey, F. A., S. Huang, J. Blichert-Toft, M. Regelous, and M. Boyet (2005), Origin of depleted components in basalt related to the Hawaiian hot spot: Evidence from isotopic and incompatible element ratios, *Geochem. Geophys. Geosyst.*, *6*, Q02L07, doi:10.1029/2004GC000757.

Garcia, M., D. Grooms, and J. Naughton (1987), Petrology and geochronology of volcanic rocks from seamounts along and near the Hawaiian ridge, *Lithos*, *20*(4), 323–336.

Green, D. H. (2000), Magmatism originating in the upper mantle, paper presented at International School on Earth

and Planetary Sciences Siena: Crust-Mantle Interactions, Siena, Italy.

Green, T. H. (1994), Experimental studies of trace-element partitioning applicable to igneous petrogenesis — Sedona 16 years later, *Chem. Geol.*, *117*, 1–36.

Grigg, R. W., and A. T. Jones (1997), Uplift caused by lithospheric flexure in the Hawaiian Archipelago as revealed by elevated coral deposits, *Mar. Geol.*, *141*, 11–25.

Guillou, H., M. O. Garcia, and L. Turpin (1997), Unspiked K-Ar dating of young volcanic rocks from the Loihi and Pitcairn seamounts, *J. Volcanol. Geotherm. Res.*, *78*, 239–249.

Gurriet, P. (1987), A thermal model for the origin of post-erosional alkalic lava, Hawaii, *Earth Planet. Sci. Lett.*, *82*, 153–158.

Hauri, E. H. (1996), Major-element variability in the Hawaiian mantle plume, *Nature*, *382*, 415–419.

Hauri, E. H., J. C. Lassiter, and D. J. DePaolo (1996), Osmium isotope systematics of drilled lavas from Mauna Loa, Hawaii, *J. Geophys. Res.*, *101*(B5), 11,793–11,806.

Hieronymus, C. F., and D. Bercovici (1999), Discrete alternating hotspot islands formed by interaction of magma transport and lithospheric flexure, *Nature*, *397*, 604–607.

Hieronymus, C. F., and D. Bercovici (2001), Focusing of eruptions by fracture wall erosion, *Geophys. Res. Lett.*, *28*, 1823–1826.

Hirschmann, M. M. (2000), Mantle solidus: Experimental constraints and the effects of peridotite composition, *Geochem. Geophys. Geosyst.*, *1*(10), doi:10.1029/2000GC000070.

Hirschmann, M. M., and E. M. Stolper (1996), A possible role for garnet pyroxenite in the origin of the ''garnet signature'' in MORB, *Contrib. Mineral. Petrol.*, *124*, 185–208.

Hirschmann, M. M., P. D. Asimow, M. S. Ghiorso, and E. M. Stolper (1999), Calculation of peridotite partial melting from thermodynamic models of mineral melts. III. Controls on isobaric melt production and the effect of water on melt production, *J. Petrol.*, *40*(5), 831–851.

Hirschmann, M., T. Kogiso, M. B. Baker, and E. M. Stolper (2003), Alkalic magmas generated by partial melting of garnet pyroxenite, *Geology*, *31*(6), 481–484.

Huppert, H. E. (1982), The propagation of two-dimensional and axisymmetric viscous gravity currents over a rigid horizontal surface, *J. Fluid Mech.*, *121*, 43–58.

Ito, G., and J. J. Mahoney (2005), Flow and melting of a heterogeneous mantle: 1. Method and importance to the geochemistry of ocean island and mid-ocean ridge basalts, *Earth Planet. Sci. Lett.*, *230*, 29–46.

Jackson, E. D., and T. L. Wright (1970), Xenoliths in the Honolulu Volcanic Series, *J. Petrol.*, *11*, 405–430.

Jones, A. T. (1993), Review of the chronology of marine terraces in the Hawaiian Archipelago, *Quat. Sci. Rev.*, *12*, 811–823.

Katz, R. F., M. Spiegelman, and C. H. Langmuir (2003), A new parameterization of hydrous mantle melting, *Geochem. Geophys. Geosyst.*, *4*(9), 1073, doi:10.1029/2002GC000433.

Kogiso, T., M. M. Hirschmann, and P. W. Reiners (2004), Length scales of mantle heterogeneities and their relations to ocean island basalt geochemistry, *Geochim. Cosmochim. Acta*, *68*(2), 345–360.

Langmuir, C. H., J. F. Bender, A. E. Bence, G. N. Hanson, and S. R. Taylor (1977), Petrogenesis of basalts from the FAMOUS-area, Mid-Atlantic Ridge, *Earth Planet. Sci. Lett.*, *36*, 133–156.

Lassiter, J. C., and E. H. Hauri (1998), Osmium-isotope variations in Hawaiian lavas: Evidence for recycled oceanic lithosphere in the Hawaiian plume, *Earth Planet. Sci. Lett.*, *164*, 483–496.

Lassiter, J. C., E. H. Hauri, P. W. Reiners, and M. O. Garcia (2000), Generation of Hawaiian post-erosional lavas by melting of a mixed lherzolite/pyroxenite source, *Earth Planet. Sci. Lett.*, *178*, 269–284.

Li, X., R. Kind, K. Priestley, S. V. Sobolev, F. Tilmann, X. Yuan, and M. Weber (2000), Mapping the Hawaiian Plume with converted seismic waves, *Nature*, *405*, 938–941.

Lipman, P. (1995), Declining growth of Mauna Loa during the last 100,000 years: Rates of lava accumulation vs. gravitational subsidence, in *Mauna Loa Revealed: Structure, Composition, History, and Hazards*, *Geophys. Monogr. Ser.*, vol. 92, edited by J. M. Rhodes and J. P. Lockwood, pp. 45–80, AGU, Washington, D. C.

Lipman, P., D. A. Clague, J. G. Moore, and R. T. Holcomb (1989), South Arch Volcanic Field—Newly identified young lava flows on the sea floor south of the Hawaiian Ridge, *Geology*, *17*, 611–614.

Liu, M., and C. G. Chase (1991), Evolution of Hawaiian basalts: A hotspot melting model, *Earth Planet. Sci. Lett.*, *104*, 151–165.

Macdonald, G. A., and T. Katsura (1964), Chemical composition of Hawaiian lavas, *J. Petrol.*, *5*, 82–133.

Macdonald, G. A., A. T. Abbot, and F. L. Peterson (1983), *Volcanoes in the Sea: The Geology of Hawaii*, 2nd ed., Univ. of Hawaii Press, Honolulu.

McBirney, A. R. (1993), *Igneous Petrology*, 2nd ed., 508 pp., Jones and Bartlett, Boston, Mass.

McKenzie, D. P. (1985), ^{230}Th-^{238}U disequilibrium and the melting processes beneath the ridge axes, *Earth Planet. Sci. Lett.*, *72*, 149–157.

McKenzie, D., and R. K. O'Nions (1991), Partial melt distribution from inversion of rare earth element concentrations, *J. Petrol.*, *32*, 1021–1091.

McNutt, M. K. (1984), Lithospheric flexure and thermal anomalies, *J. Geophys. Res.*, *89*(B13), 11,180–11,194.

McNutt, M., and W. H. Menard (1978), Lithospheric flexure and uplifted atolls, *J. Geophys. Res.*, *83*, 1206–1212.

Moore, J. G. (1970), Relationship between subsidence and volcanic load, Hawaii, *Bull. Volcanol.*, *34*, 563–576.

Moore, J. G., D. A. Clague, and W. R. Normark (1982), Diverse basalt types from Loihi Seamount, Hawaii, *Geology*, *10*, 88–92.

Muller, J. R., G. Ito, and S. J. Martel (2001), Effects of volcano loading on dike propagation in an elastic half space, *J. Geophys. Res.*, *106*(B6), 11,101–11,113.

Mysen, B. O., and I. Kushiro (1977), Compositional variation of coexisting phases with degree of melting of peridotite in the upper mantle, *Am. Mineral.*, *62*, 843–865.

Nadai, A. (1931), *Theory of Flow and Fracture of Solids*, 260–269 pp., McGraw-Hill, New York.

Okano, O., and M. Tatsumoto (1996), Petrogenesis of ultramafic xenoliths from Hawaii inferred from Sr, Nd, and Pb isotopes, in *Earth Processes: Reading the Isotopic Code*, *Geophys. Monogr. Ser.*, vol. 95, edited by A. Basu and S. Hart, pp. 135–147, AGU, Washington, D. C.

Ozawa, A., T. Tagami, and M. Garcia (2005), Unspiked K-Ar dating of the Honolulu rejuvenated and Ko'olau shield volcanism on O'ahu, Hawai'i, *Earth Planet. Sci. Lett.*, *232*(1–2), 1–11.

Pertermann, M., and M. M. Hirschmann (2003), Partial melting experiments on a MORB-like pyroxenite between 2 and 3 GPa: Constraints on the presence of pyroxenite in

basalt source regions from solidus location and melting rate, *J. Geophys. Res.*, *108*(B2), 2125, doi:10.1029/2000JB000118.

Phipps Morgan, J. (2001), Thermodynamics of pressure release melting of a veined plum pudding mantle, *Geochem. Geophys. Geosyst.*, *2*(4), doi:10.1029/2000GC000049.

Pietruszka, A. J., K. H. Rubin, and M. Garcia (2001), ^{226}Ra-^{230}Th-^{238}U disequilibria of historical Kilauea lavas (1790–1982) and the dynamics of mantle melting within the Hawaiian plume, *Earth Planet. Sci. Lett.*, *186*, 15–31.

Plank, T., M. Spiegelman, C. H. Langmuir, and D. W. Forsyth (1995), The meaning of "mean F": Clarifying the mean extent of melting at ocean ridges, *J. Geophys. Res.*, *100*(B8), 15,045–15,052.

Priestley, K., and F. Tilmann (1999), Shear-wave structure of the lithosphere above the Hawaiian Hot Spot from two-station Rayleigh wave phase velocity measurements, *Geophys. Res. Lett.*, *26*, 1493–1496.

Quane, S., M. O. Garcia, H. Guillou, and T. Hulsebosch (2000), Magmatic history of Kilauea Volcano based on drill core from SOH1: Implications for the structure of the Hawaiian Plume, *J. Volcanol.*, *102*(3–4), 319–338.

Reiners, P. W., and B. K. Nelson (1998), Temporal-compositional-isotopic trends in rejuvenated-stage magmas of Kauai, Hawaii, and implications for mantle melting processes, *Geochim. Cosmochim. Acta*, *62*, 2347–2368.

Ribe, N. M., and U. R. Christensen (1999), The dynamical origin of Hawaiian volcanism, *Earth Planet. Sci. Lett.*, *171*, 517–531.

Roden, M. F., F. A. Frey, and D. A. Clague (1984), Geochemistry of tholeiitic and alkalic lavas from the Koolau Range, Oahu, Hawaii: Implications for Hawaiian volcanism, *Earth Planet. Sci. Lett.*, *62*, 215–228.

Satake, K., J. R. Smith, and K. Shinozaki (2002), Three-dimensional reconstruction and tsunami model of the Nuuanu and Wailau landslides, Hawaii, in *Hawaiian Volcanoes: Deep Underwater Perspectives*, *Geophys. Monogr. Ser.*, vol. 128, edited by E. Takahashi et al., pp. 333–346, AGU, Washington, D. C.

Sims, K. W. W., D. DePaolo, M. T. Murrell, W. Baldridge, S. Goldstein, D. A. Clague, and M. Jull (1999), Porosity of the melting zone and variations in the solid mantle upwelling rate beneath Hawaii: Inferences from ^{238}U-^{230}Th-^{226}Ra and ^{235}U-^{231}Pa disequilibria, *Geochim. Cosmochim. Acta*, *63*(23/24), 4119–4138.

Smith, J. R., and P. Wessel (2000), Isostatic consequences of giant landslides on the Hawaiian Ridge, *Pure Appl. Geophys.*, *157*, 1097–1114.

Sneddon, I. N. (1951), *Fourier Transforms*, 1st ed., International Series in Pure and Applied Mathematics, 542 pp., McGraw-Hill, New York.

Staudigel, H., S. Hart, A. Zindler, M. Lanphyre, C.-Y. Chen, and D. A. Clague (1984), Pb, Nd, Sr isotopes of Loihi Seamount, Hawaii, *Earth Planet. Sci. Lett.*, *69*, 13–29.

Stearns, H. T. (1967), *Geology of the Hawaiian Islands*, 2nd printing, *Hawaii Div. of Hydrogr. Bull. 8*, 112 pp.

Stearns, H. T. (1978), Quaternary shorelines in the Hawaiian Islands, *Bishop Mus. Bull.*, *237*, 1–57.

Sun, S.-S., and W. F. McDonough (1989), Chemical and isotopic systematics of oceanic basalts: Implications for mantle compositions and processes, in *Magmatism in the Ocean Basins*, edited by A. D. Saunders and M. J. Norry, *Geol. Soc. Spec. Publ.*, *42*, 313–345.

Tagami, T., Y. Nishimitsu, and D. R. Sherrod (2003), Rejuvenated-stage volcanism after 0.6-m. y. quiescence at West Maui Volcano, Hawaii: New evidence from K-Ar ages and chemistry of Lahaina Volcanics, *J. Volcanol. Geotherm. Res.*, *120*(3–4), 207–214.

ten Brink, U. S., and T. M. Brocher (1987), Multichannel seismic evidence for a subcrustal intrusive complex under Oahu and a model for Hawaiian volcanism, *J. Geophys. Res.*, *92*(B13), 13,687–13,707.

Turcotte, D. L., and G. Schubert (2002), *Geodynamics*, 2nd ed., 456 pp., Cambridge Univ. Press, New York.

Walker, G. P. L. (1990), Geology and volcanology of the Hawaiian Islands, *Pac. Sci.*, *44*(4), 315–347.

Watts, A. B., and U. S. ten Brink (1989), Crustal structure, flexure, and subsidence of the Hawaiian Islands, *J. Geophys. Res.*, *94*, 10,473–10,500.

Watts, A. B., U. S. ten Brink, P. Buhl, and T. M. Brocher (1985), A multichannel seismic study of lithospheric flexure across the Hawaiian-Emperor Seamount Chain, *Nature*, *315*, 105–111.

Wessel, P. (1993), A reexamination of the flexural deformation beneath the Hawaiian Islands, *J. Geophys. Res.*, *98*(B7), 12,177–12,190.

Wilson, J. T. (1963), A possible origin of the Hawaiian Islands, *Can. J. Phys.*, *41*, 863–870.

Woods, M., and E. Okal (1996), Rayleigh-wave dispersion along the Hawaiian swell: A test of lithospheric thinning by thermal rejuvenation at a hot spot, *Geophys. J. Int.*, *125*, 325–339.

Woods, M., J. J. Lévêque, E. Okal, and M. Cara (1991), Two-station measurements of Rayleigh wave group velocity along the Hawaiian swell, *Geophys. Res. Lett.*, *18*, 105–108.

Yang, H.-J., F. A. Frey, and D. A. Clague (2003), Constraint on the source components of lavas forming the Hawaiian North Arch and Honolulu volcanics, *J. Petrol.*, *44*(4), 603–627.

Zou, H. (1998), Trace element fractionation during modal and nonmodal dynamic melting and open-system melting: A mathematical treatment, *Geochim. Cosmochim. Acta*, *62*(11), 1937–1945.